

AMERICAN UNIVERSITY OF BEIRUT

Relaxational Dynamics and Compressional  
Properties of Polymer Brushes

by

Carmen Ghassan Al Masri

A thesis

submitted in partial fulfillment of the requirements  
for the degree of Master of Science  
to the Department of Physics  
of the Faculty of Arts and Sciences  
at the American University of Beirut


Beirut, Lebanon  
July 2020

AMERICAN UNIVERSITY OF BEIRUT

Relaxational Dynamics and Compressional  
Properties of Polymer Brushes

by  
Carmen Ghassan Al Masri

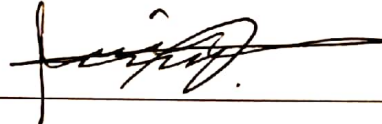
Approved by:



Dr. Leonid Klushin, Professor

Advisor

Physics



Dr. Jihad Touma, Professor

Member of Committee

Physics



Dr. Michel Kazan, Associate Professor

Member of Committee

Physics

Date of thesis defense: February 5, 2020

# AMERICAN UNIVERSITY OF BEIRUT

## THESIS, DISSERTATION, PROJECT RELEASE FORM

Student Name: AL HASRI Carmen Ghassan  
Last First Middle

Master's Thesis       Master's Project       Doctoral Dissertation

I authorize the American University of Beirut to: (a) reproduce hard or electronic copies of my thesis, dissertation, or project; (b) include such copies in the archives and digital repositories of the University; and (c) make freely available such copies to third parties for research or educational purposes.

I authorize the American University of Beirut, to: (a) reproduce hard or electronic copies of it; (b) include such copies in the archives and digital repositories of the University; and (c) make freely available such copies to third parties for research or educational purposes after: **One \_\_\_ year from the date of submission of my thesis, dissertation or project.**

**Two \_\_\_ years from the date of submission of my thesis , dissertation or project.**

**Three \_\_\_ years from the date of submission of my thesis , dissertation or project.**

elamunhasri  
Signature

07/07/2020  
Date

This form is signed when submitting the thesis, dissertation, or project to the University Libraries

# Acknowledgements

I would like to first thank my advisor Professor Leonid Klushin for all the guidance, insights and support. The hours spent discussing difficult concepts and his attention to the smallest details helped me grow both as a person and a scientist. I also thank the committee members, Professors Jihad Touma and Michel Kazan, for all their feedback and their help whenever I reached out. In addition, I would like to extend my thanks to my colleagues, in particular Rodrigue Badr, whose mentoring and encouragement enormously helped with the thesis progress. Thanks also to Kafa Alameh and Wassim Sleiman, for being part of this journey from the very start and providing both insightful discussions and fun times.

Additionally, I'm thankful for everyone in the graduate room, including Ashod Khederlarian, Aisha Al Rifaii, Ahmad Lalti, Ghina Al Atat, Ibrahim Nouredine and Hassan Taki for all the good memories and positive atmosphere that made the experience much more enjoyable. A special thanks to Aya Sakaya and Hadi Dayekh for their invaluable friendship and the countless good times spent together.

Above all, I would like to thank my family, and in particular my parents, for all their patience and unconditional support, without which none of this would have been possible.

# An Abstract of the Thesis of

Carmen Ghassan Al Masri for Master of Science  
Major: Physics

Title: Relaxational Dynamics and Compressional Properties of Polymer Brushes

We run molecular dynamics simulations to study the relaxation dynamics of a single polydisperse brush in the short unentangled regime, and of a brush-bilayer system of different polydispersity indices to study its equilibrium pressure properties. We find an unexpected behaviour with the relaxation times, likely due to the effects of frozen disorder. As for the pressure of the bilayer system, we found that the characterization of the free energy by the number of interbrush contacts is a valid one. However, we found that the pressure for the same densities depended on the polydispersity index. Investigations led us to attribute this to chain-end effects, which were completely unaccounted for in the context of the mean field theory.

# Contents

<b>Acknowledgements</b>	<b>v</b>
<b>Abstract</b>	<b>vi</b>
<b>1 Introduction</b>	<b>1</b>
<b>2 Literature Review</b>	<b>4</b>
2.1 Properties of Real and Ideal Polymer Chains . . . . .	4
2.1.1 Ideal Chains . . . . .	4
2.1.2 Free Energy of an Ideal Chain . . . . .	5
2.1.3 Excluded Volume Interactions . . . . .	7
2.1.4 Flory Theory for Real Chains . . . . .	7
2.2 Osmotic Pressure . . . . .	9
2.2.1 Free Energy of Mixing . . . . .	9
2.2.2 Application to Osmotic Pressure . . . . .	10
2.3 Evaluating Pressure in a Brush Bilayer . . . . .	13
2.3.1 Normal Pressure from the Free Energy . . . . .	13
2.3.2 Normal Pressure from the Equation of State . . . . .	14
2.3.3 Interaction free Energy from Interbrush Contacts . . . . .	15
2.4 Modelling Chain Dynamics . . . . .	18
2.4.1 The Dumbbell Model . . . . .	18
2.4.2 Properties of the Rouse Chains . . . . .	19
2.5 Relaxation Dynamics of a Monodisperse Brush . . . . .	21
2.5.1 Initial Description for Chain Relaxation . . . . .	21
2.5.2 Later Discoveries and Modifications . . . . .	21
2.6 Models and Methods . . . . .	24
2.6.1 The Model . . . . .	24
2.6.2 Model of a Polydisperse Brush . . . . .	26
2.6.3 Microscopic Pressure Tensor . . . . .	28
<b>3 Results</b>	<b>30</b>
3.1 Relaxation times . . . . .	30
3.1.1 Monodisperse Brush . . . . .	30

3.1.2	Polydisperse Brush . . . . .	33
3.2	Pressure and Interaction Free Energy . . . . .	37
3.2.1	Equation of state of a WCA gas . . . . .	37
3.2.2	Compressing a Monodisperse Brush Bilayer . . . . .	38
3.2.3	Interaction Free Energy . . . . .	41
3.2.4	Equation of State for Oligomers . . . . .	43
3.2.5	Chain End Effects in Brush Bilayers . . . . .	46
3.3	Conclusions and Future Work . . . . .	50

# List of Figures

1.1	Schematic of a compressed polymer-brush bilayer. The free energy in the interpenetration zone of width $l$ can be quantified through concentration blobs, each bringing energy of the order $kT$ to the system. . . . .	2
2.1	An Ideal Chain . . . . .	4
2.2	Renormalized ideal chain, with effective monomers shown in blue. . . . .	5
2.3	The volume not available to the center of the sphere B is a sphere of radius $D$ . . . . .	7
2.4	Lattice model for a polymer chain in a solution. The sites occupied by the monomers are shown in black, and those occupied by the solvent in blue. . . . .	9
2.5	Direction of flow from compartment B (pure solvent) to compartment A (polymers and solvent) . . . . .	10
2.6	A Brush Bilayer . . . . .	13
2.7	density profile of the brush bilayer system for $k = 1.05$ at walls separation $D = 30$ . The inset shows the overlap region, given by $\Gamma = \phi_1\phi_2$ in which the brushes interpenetrate . . . . .	16
2.8	Schematic of a compressed polymer-brush bilayer. The free energy in the interpenetration zone of width $l$ can be quantified through concentration blobs, each bringing energy of the order $kT$ to the system. . . . .	16
2.9	Change in the conformation of the chain in bead-spring model [1]. . . . .	18
2.10	Spring force on bead $n$ [1]. . . . .	18
2.11	Brush in the coil regime (left) and in the stretched regime (right) . . . . .	21
2.12	Schulz-Zimm distribution for $N_n = 100$ and $N_w/N_n = 1.02, 1.15, 3$ . . . . .	27
2.13	The Irving-Kirkwood contour. In each slice, the interaction force contributes a fraction $\lambda_i$ to the configurational part of the stress tensor . . . . .	29



3.2	3.1a shows correlation functions in $x$ and $z$ vs the time intervals $\tau$ (in natural units). Figure 3.1c shows the fluctuations in $x$ and $z$ vs the number of monomers per chain $N$ on a loglog scale. The dashed lines represent the linear fits from which a slope of 2.0 was extracted for the $z$ component and 1.0 for the $x$ component, in accordance with the Rouse model. The solid lines represent the theoretical curves for the fluctuations in $x$ and $z$ . Figure 3.1d shows the relaxation times in $x$ and $z$ vs $N$ , with linear fits (dashed lines) for the $z$ -component from which a slope of $3.0 \pm 0.1$ was obtained, and a slope of $2.3 \pm 0.3$ for the $x$ -component. These power laws are also consistent with those predicted by the Rouse model ( $\tau_z \sim N^3$ and $\tau_x \sim N^2$ ) . . . . .	32
3.3	Average density profile of a monodisperse brush with $n_c = 25$ and $N_n = 20$ along $z$ . The binning was done along slices of width $0.1\sigma$ . The fit is obtained from the analytical form, where we set $v = 3.6$ and $\sigma = 1/9$ . . . . .	32
3.4	Average density profile of a monodisperse (blue) and polydisperse (red) brush with $n_c = 25$ and $N_n = 15$ along $z$ . The binning was done along slices of width $0.1\sigma$ . . . . .	33
3.5	mean positions and fluctuations of chain ends . . . . .	34
3.6	figure 3.1a shows the relaxation times for $N_w/N_n = 1.15$ , $N_n = 10, 15, 20$ . . . . .	36
3.7	log-log plot of the total pressure vs monomer density for a gas of $N = 500$ monomers interacting through a WCA potential . . . . .	38
3.8	different components of the pressure tensor along the $z$ axis for a monodisperse brush before interpenetration. The ideal contribution can be recovered from the momenta of the particles (top left), or equivalently from the density profile of the brush (bottom left). The forces contribution (WCA and KG) can be seen on the top right, and the total pressure due to both contributions on the bottom right. . . . .	39
3.9	normal and lateral components of pressure tensor after compression. An interpenetration zone is established and the total pressure is positive. . . . .	39
3.10	pressure computed from the microscopic pressure tensor (blue line), and from computing the net force exerted by the walls and dividing by the area of the surfaces (yellow points) . . . . .	40
3.11	total interaction free energy vs number of interbrush contacts for brushes of polydispersity indices $k = 1, 1.05, 1.1, 2$ . The maximum midplane density reached was about 0.6. . . . .	42
3.12	log-log plot of the average pressure vs the minimum density along $z$	42
3.13	log-log plot of the pressure vs the average density along $z$ for a solution of $n_c = 9$ chains of lengths $N = 2, 5, 10, 15, 25$ . . . . .	44

3.14	Pressure vs chain length at melt density $\phi = 0.8$ . . . . .	44
3.16	number density in the overlap region vs distance $z$ from surface fitted using $\Gamma = \left(\frac{\phi_0}{2}\right)^2 \cosh^2\left(\frac{z-z_0}{l}\right)$ , with $\phi_0 = 0.12$ and $z_0 = 14$ . . . . .	46
3.17	interpenetration length $l$ vs minimum density in the brush profile. . . . .	47
3.18	fraction of chain ends in the interpenetration zone vs the minimum density along $z$ for $k = 1, 1.05, 1.1, 2$ . . . . .	47
3.19	pressure vs fraction of chain ends in polymer solutions (solid lines) and brush bilayers (stars) . . . . .	48
3.20	pressure vs minimum density in polymer solutions (solid lines) and brush bilayers (stars) . . . . .	49

# Chapter 1

## Introduction

Polymer brushes are formed when polymer chains are grafted to a surface at a sufficiently high density. They have applications in a wide scope of fields ranging from biomedicine (drug delivery, tissue engineering scaffolds, biomedical probes, etc...), to antifouling surfaces, colloidal stabilization and tribology (lubrication)[2, 3, 4]. With such a diverse range of applications, it became necessary to understand both the equilibrium and dynamical properties of these polymeric structures, particularly that of the fundamental densely grafted monolayer. While the equilibrium properties of these monolayers have been extensively studied both theoretically and experimentally[5, 6], the dynamical properties (and particularly relaxation dynamics) remain to be fully explored.

It had been theorized that for long chains, the relaxation times in the direction normal to the grafting surface scaled as  $\tau_z \sim \rho^{2/3}N^3$  while in the lateral direction they scaled as  $\tau_{\parallel} \sim \rho^{-1/6}N^2$ , where  $N$  is the index of polymerization and  $\rho$  the grafting density [7]. This scaling took into account the anomalous chain-end fluctuations, due to the last monomers of each chain exploring the entire space within the brush thickness [7]. However, after recently conducting molecular dynamics and Monte Carlo simulations, it was apparent that for chains with a large enough degree of polymerization ( $N \geq 64$ ), the relaxation times in the lateral and normal directions strongly deviated from the theoretical predictions, and were shown to both have the same  $N$ -dependence that scales as  $\tau \sim N^{3.7}$  [8]. The deviation in the normal direction from the  $N^3$  dependence was attributed to the previously unaccounted-for entanglement effects. As for the lateral direction, the high discrepancy was attributed to fluctuations of the  $z$ -component being coupled with those of the  $xy$  components of the chains [8]. However, whether this coupling in the fluctuations still exists in the regime of short, unentangled chains remains an open question.

On the other hand, in the case of polydisperse chains, it was theoretically predicted that even for very small polydispersity, the anomalous chain-end fluctuations become suppressed; the end of each chain exhibits gaussian fluctuations, from which we can recover relaxation times that scale as  $\tau_{polydisperse} \sim N^2 p^{-1/2}$ ,

where  $p$  is the index of polydispersity [2]. However, this prediction has yet to be tested by simulation. We therefore propose to conduct molecular dynamics simulations to study the relaxation times of both monodisperse and polydisperse brushes in the short, unentangled regime and compare their behaviors.

Another system that will be of interest to us is the polymer-brush bilayer, which was shown to be the most effective coating to achieve low-friction forces between surfaces, and therefore provides extraordinary lubrication properties and plays an important role in colloidal stabilization [4]. Hence, understanding the equilibrium properties of these bilayers is necessary. Of particular interest to us is the compressive force felt by the chains when the individual brushes are brought together and start interpenetrating. A sketch of the situation is shown in figure 1.1 [3].

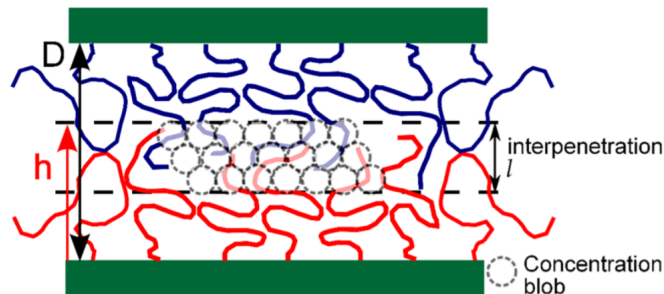


Figure 1.1: Schematic of a compressed polymer-brush bilayer. The free energy in the interpenetration zone of width  $l$  can be quantified through concentration blobs, each bringing energy of the order  $kT$  to the system.

One approach to evaluate the pressure in this system involves evaluating its total free energy, from which the pressure would be recovered by taking the derivative of the free energy per unit area  $F$  with respect to the separation between the brushes ( $dF/dD = P$ ). A recent study [3] estimated the free energy inside interpenetration zone only, and from it recovered the total free energy of the system, thus relating the free energy (and hence the osmotic pressure) to the depth of the interpenetration  $l$ . However, this study is based on an assumption in which the free energy of the system was a function of the number of interbrush contacts, which is a questionable assumption that we will attempt to verify in this work.

Alternatively, one can simply express the pressure as a function of the local number density through an equation of state. Recent studies [9] using the self-consistent field (SCF) theory showed the equivalence between this characterization of pressure and the pressure from the free energy. However, no systematic study using MD simulations has been conducted yet. We therefore propose to run molecular dynamics simulations on brush-bilayer systems of different polydispersity indices to check the consistency of the pressure characterization as we

currently understand it, which will serve to guide our theoretical understanding of it.

# Chapter 2

## Literature Review

### 2.1 Properties of Real and Ideal Polymer Chains

#### 2.1.1 Ideal Chains

The starting point of most polymer chain models is that of a flexible, freely jointed ideal chain. In this model, the interaction between monomers separated by a sufficient number of bonds along the chain is neglected, and all bonds are of the same length, with directions independent of each other. [10] We consider a polymer chain with  $n$  monomers  $A_i$ , with  $0 \leq i < n$  (Figure 2.1).

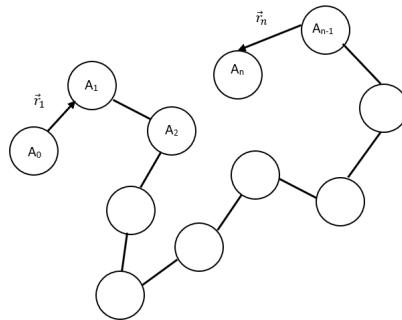


Figure 2.1: An Ideal Chain

The end-to-end vector  $\mathbf{R}_n$  connecting  $A_0$  to  $A_n$  is then given by

$$\mathbf{R}_n = \sum_1^n \mathbf{r}_i \quad (2.1)$$

Since there is no preferred orientation of the chain, the ensemble average of the end-to-end vector is zero  $\langle \mathbf{R} \rangle = 0$ . The simplest quantity to describe the average size of the polymer chain is then given by the mean-square end-to-end distance:

$$\langle \mathbf{R}_n^2 \rangle = \sum_1^n \langle \mathbf{r}_i^2 \rangle + 2 \sum_{1 \leq i < j \leq n} \langle \mathbf{r}_i \mathbf{r}_j \rangle$$

If all the bond vectors were independent of each other, there would be no correlations between two different bond vectors, hence  $\langle \mathbf{r}_i \mathbf{r}_j \rangle = 0$ . However, in a typical polymer chain the consecutive bonds are correlated. The correlation only dies out when the bond vectors are distant enough, so that  $\lim_{|i-j| \rightarrow \infty} \langle \mathbf{r}_i \mathbf{r}_j \rangle = 0$  [11].

We can thus renormalize the chain into  $N$  independent segments of length  $b$ , over which there is no correlation between the bonds. We thus obtain an equivalent freely jointed polymer brush of  $N$  effective monomers of length  $b$ , known as Kuhn monomers (Figure 2.2) [11]. Keeping the maximum end-to-end distance and

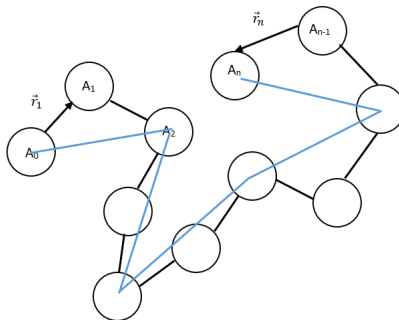


Figure 2.2: Renormalized ideal chain, with effective monomers shown in blue.

mean-square end-to-end distance fixed, we obtain the following renormalization conditions:

$$R_{max} = Nb$$

$$\langle \mathbf{R}_n^2 \rangle = \sum_1^N \langle \mathbf{r}_i^2 \rangle + 2 \sum_{1 \leq i < j \leq N} \langle \mathbf{r}_i \mathbf{r}_j \rangle = Nb^2$$

We find that the configurations of the freely jointed ideal chain can be mapped to a random walk, with  $N$  steps the size of a Kuhn monomer. This property, along with other properties that will be discussed in the following sections, is universal to all flexible polymers, independent of their chemical constitution [10]. We now turn to studying the free energy of such chains.

### 2.1.2 Free Energy of an Ideal Chain

We consider, as in the previous section, a flexible polymer chain with  $N$  equivalent Kuhn monomers of length  $b$ . Since the chain follows a random walk configuration, the probability distribution of its end-to-end distance will be a Gaussian

centered about  $\mathbf{R} = 0$ . Therefore, for  $N \gg 1$ , the three-dimensional probability distribution function for the end-to-end vector  $\mathbf{R}$  is given by[11]:

$$P_{3D}(N, \mathbf{R}) = \left( \frac{3}{2\pi Nb^2} \right)^{3/2} \exp \left( -\frac{3\mathbf{R}^2}{2Nb^2} \right) \quad (2.2)$$

This probability distribution function, being proportional to the number of configurations  $\Omega$  of a freely jointed chain of  $N$  monomers with end-to-end distance  $\mathbf{R}$ , enables us to write the configurational entropy of a polymer chain as a function of its end-to-end distance:

$$S(\mathbf{R}) = k \ln \Omega(\mathbf{R}) = -\frac{3k\mathbf{R}^2}{2Nb^2} + \text{constant} \quad (2.3)$$

Where  $k$  is the Boltzmann constant. We can see that a stretching of the polymer chain beyond its ideal length will lead to a decrease in the entropy, as there are fewer possible configurations than when the chain is unperturbed.

The Helmholtz free energy with energy  $U$  and absolute temperature  $T$  is  $F(\mathbf{R}) = U(\mathbf{R}) - TS(\mathbf{R})$ . However, monomers of an ideal chain have no interaction energy, so  $U$  is independent of the end-to-end vector  $\mathbf{R}$ . We can thus write the free energy as:

$$F(\mathbf{R}) = \frac{3kT\mathbf{R}^2}{2Nb^2} + \text{constant} \quad (2.4)$$

We find that stretching the chain results in an increase of the free energy quadratic in  $\mathbf{R}$ . This means that stretching a chain by a distance  $R$  results in a restoring force linear in  $R$  [11]:

$$\mathbf{f} = -\frac{\partial F}{\partial \mathbf{R}} = -\frac{3kT}{Nb^2} \mathbf{R} \quad (2.5)$$

The entropic elasticity of a chain therefore satisfies Hook's law, with spring constant  $3kT/Nb^2$ .

So far, we assumed that monomers could overlap, and that there is no energetic cost to their interactions. However, in most cases, monomers of real chains do interact, which would affect the properties of that chain. We study these properties in the next section.



### 2.1.3 Excluded Volume Interactions

So far, we have assumed that monomers in a chain cannot interact with each other, which would make overlap possible. However, two monomers of a real chain cannot occupy the same volume in space, as shown by figure 2.3); If we represent the monomers as hard spheres, their center-to-center distance cannot be less than  $D$ , the diameter of the monomer. The excluded volume  $v$  is then the sphere of radius  $D$ , given by  $v = \int 4\pi r^2 dr$ . [1]

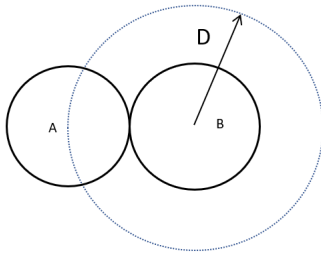


Figure 2.3: The volume not available to the center of the sphere  $B$  is a sphere of radius  $D$

In addition to this hard-core repulsion, there is also an energy cost  $U(r)$  of bringing two monomers within a distance  $r$  of each other. The excluded volume would then relatively increase if the net interaction is repulsive and decrease if it is negative [1].

The probability of finding two monomers within that distance  $r$  is weighted by the Boltzmann factor  $\exp[-U(r)/kT]$ . We can then express the excluded volume as [11]:

$$v = \int 4\pi r^2 (1 - \exp[-U(r)/kT]) dr \quad (2.6)$$

Note that in the case of a bad solvent, monomer-monomer attraction dominates and  $v$  can take a negative value. For our purposes, we only consider the case of a good solvent where  $v > 0$ .

The excluded volume will significantly affect the properties of the polymer chains, as we will see in the next sections.

### 2.1.4 Flory Theory for Real Chains

We now study the properties of a real chain with  $N$  Kuhn monomers occupying the effective volume  $v$ . Since monomer overlap is no longer possible, there will be an entropic repulsion between the monomers that would lead to the swelling of the real chain relative to the ideal chain; the real chains follow a self-avoiding walk [10]. The simplest way to characterize the energy of such a chain is given

by the Flory theory, which takes into account the interplay of the entropic and interaction energies.

To estimate the repulsion energy of the real chain, we adopt a Mean-Field theory approach where the monomers are distributed uniformly within the volume occupied by the chain ( $V \approx R^3$ ). The probability of a monomer being within the excluded volume of another monomer is the product of  $v$  and the number density of the monomers  $N/R^3$ . The energetic cost of each exclusion is  $kT$ , so the total energetic interaction for  $N$  monomers is given by:

$$F_{int} = kTv \frac{N^2}{R^3} \quad (2.7)$$

The stretching of the chain, which reduces monomer-monomer contacts, is then energetically favorable. However, as we saw in section 2.1.2, there is an entropic loss associated with this stretching. The equilibrium configuration of the chain is a balance between these two effects, captured by the Flory theory, in which the free energy is a combination of the entropic and interaction free energies. Combining eq 2.4 and 2.7, we obtain:

$$F = \frac{3kTR^2}{2Nb^2} + kTv \frac{N^2}{R^3} \quad (2.8)$$

Minimizing the free energy with respect to  $R$  gives the optimal size of the chain, which scales as  $R \approx v^{1/5} b^{2/5} N^{3/5}$ .

This power law dependence of  $R$  on  $N$  is universal to all real chains under good solvent conditions. In this work, we will be exclusively dealing with such chains. In section 2.3, we turn to characterizing the free energy in our system of interest, with 2.8 as a basis. In the next section, we give a brief explanation of the osmotic pressure in relation to polymer solutions.

## 2.2 Osmotic Pressure

### 2.2.1 Free Energy of Mixing

Suppose that we mix into a solvent polymer chains. We assume a homogeneous distribution where the mean field assumption holds. A simple way to determine the change in free energy due to mixing was developed by Flory and Huggins [12]. We first consider a lattice with  $n_s$  solvent molecules and  $n_p$  polymer chains of length  $N$  (Figure 2.4). The total number of sites is then  $n_t = n_s + Nn_p$ . Assuming both monomers and solvents occupy sites of equal volume, the volume fraction of the solvent is given by  $\phi_s = n_s/n_t$  and that of the polymer by  $\phi_p = Nn_p/n_t$ . Before mixing, a single solvent molecule could occupy  $\Omega_s = n_t\phi_s$  states (possible lattice positions). After mixing, the number of states becomes  $\Omega_{s+p} = n_t$ . The change of entropy for one solvent molecule is then  $\Delta S_s = k \ln \Omega_{s+p} - k \ln \Omega_s = -k \ln \phi_s$ . Adding the entropy contribution of each molecule, we finally obtain [13]:

$$\Delta S_{mix}/n_t = \phi_s \ln \phi_s + \frac{\phi_p}{N} \ln \phi_p \quad (2.9)$$

We find that mixing always increases the entropy of the system. One should note that for very large chains ( $N \rightarrow \infty$ ) the polymer contribution becomes negligible, and the change in entropy is largely dominated by the solvent contribution.

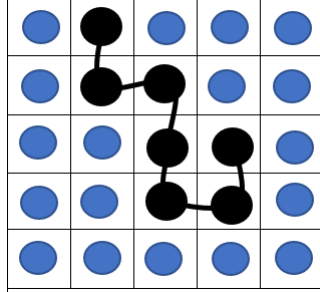


Figure 2.4: Lattice model for a polymer chain in a solution. The sites occupied by the monomers are shown in black, and those occupied by the solvent in blue.

Now we wish to find the energy of mixing  $U_{mix}$ . We consider 3 interaction energies: solvent-solvent interactions  $\epsilon_{ss}$ , polymer-polymer interactions  $\epsilon_{pp}$  and polymer-solvent interactions  $\epsilon_{ps}$ . If each site has  $z$  neighbouring sites, the energy before mixing is given by  $U_0 = z/2(\phi_s\epsilon_{ss} + \phi_p\epsilon_{pp})$ . [14] After mixing, the energy of interaction becomes  $U_{s+p} = z/2(\phi_s^2\epsilon_{ss} + \phi_p^2\epsilon_{pp} + 2\phi_s\phi_p\epsilon_{sp})$ . Subtracting  $U_{s+p}$  from  $U_0$ , and using  $\phi_s + \phi_p = 1$ , one finally obtains [14]

$$U_{mix} = kT\chi\phi_p\phi_s \quad (2.10)$$

Where  $\chi = z/2kT(2\epsilon_{sp} - \epsilon_{ss} - \epsilon_{pp})$  is called the "interaction parameter". It is a measure of energy change when we exchange a solvent molecule for a monomer.

In a good solvent, mixing is promoted by the fact that it is more energetically favourable for monomers to interact with solvents than with each other (same for solvents). In that case,  $\chi < 0$ . For an ideal mixture, there is no difference in energetic cost between the 3 different interactions and  $\chi = 0$ . Combining eq. 2.10 and 2.9, the free energy change per site upon mixing  $\Delta F_{mix} = \Delta U_{mix} - T\Delta S_{mix}$  is finally given by:

$$\Delta F_{mix} = kT\left[\phi_s \ln \phi_s + \frac{\phi_p}{N} \ln \phi_p + kT\chi\phi_p\phi_s\right] \quad (2.11)$$

One should note that since  $\phi < 1$ ,  $\ln \phi < 0$ , and for a good solvent  $\chi < 0$ , mixing will always be energetically favourable and will lower the free energy of the system.

### 2.2.2 Application to Osmotic Pressure

We start by illustrating osmotic pressure with the system shown in figure 2.5: an isothermal system with two compartments are separated by a semi-permeable membrane, allowing the passage of solvent but blocking the passage of polymers. The only requirement for thermodynamic equilibrium is that the chemical potential of the solvent molecules be equal across compartments. It is not necessary for the chemical potential of polymers to be the same [15].

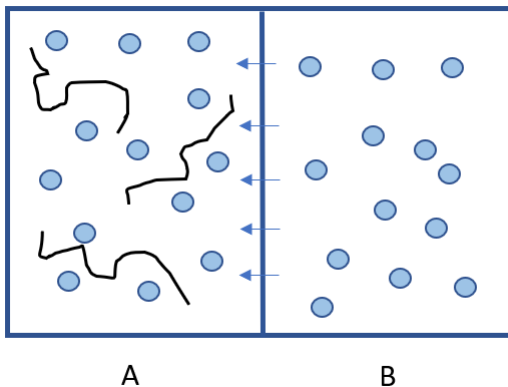


Figure 2.5: Direction of flow from compartment B (pure solvent) to compartment A (polymers and solvent)

When a polymer chain is added in compartment A, we have shown (eq. 2.11) that the resultant is a decrease in the free energy of the solvent, which translates into a decrease in its chemical potential  $\Delta\mu_s(p, T) = \mu_s(p, T) - \mu_s^0(p, T)$ , where  $\mu_s^0(p, T)$  is the chemical potential of the pure solvent. This change is given by [16]:

$$\Delta\mu_s = \frac{\partial\Delta F_{mix}}{\partial n_s}\Big|_{T, P, n_p} = kT \left[ \ln \phi_s + \left(1 - \frac{1}{N}\right) \phi_p + \chi\phi_p^2 \right] \quad (2.12)$$

Since the chemical potential of the pure solvent is higher than that with the polymers, there will be a net flow of solvent until their chemical potentials are equal. Alternatively, chemical potential can be raised if the pressure of the system is increased. The pressure required to stop the solvent flow from  $B$  to  $A$  is called the osmotic pressure of the system. We can re-write the equilibrium condition as:

$$\mu_s^0(T, P) = \mu_s(T, P + \Pi) \quad (2.13)$$

Where  $\Pi$  is the osmotic pressure. We Taylor expand to get a linear approximation at equilibrium and obtain [16]:

$$\mu_s^0(T, P) = \mu_s(T, P) + \Pi \left. \frac{\partial \mu_s}{\partial P} \right|_{T, n_s} + \mathcal{O}(2)$$

From thermodynamics, we know that  $\partial \mu_s / \partial P = V$ , where  $V$  is the molar volume of the solvent. We then get

$$\mu_s(T, P) = \mu_s^0(T, P) - V\Pi \quad (2.14)$$

Using eq. 2.12, we finally get an equation for the osmotic pressure:

$$V\Pi = kT \left[ \ln \phi_s + \left( 1 - \frac{1}{N} \right) \phi_p + \chi \phi_p^2 \right] \quad (2.15)$$

Using  $\ln \phi_s = \ln(1 - \phi_p)$ , and for small  $\phi_p$  the approximation  $\ln(1 - \phi_p) \approx -\phi_p - 1/2\phi_p^2 + \dots$ , we obtain:

$$V\Pi = kT \left[ \frac{\phi_p}{N} + \left( \frac{1}{2} - \chi \right) \phi_p^2 + \dots \right] \quad (2.16)$$

There are two things to note: first, in the dilute limit, the second-order term is negligible and we recover

$$\Pi_{\phi_p \rightarrow 0} = kT \frac{\phi_p}{N} = kT\nu \quad (2.17)$$

Where  $\nu = \phi_p/N$  is the concentration of monomers (as opposed to polymer chains). This is known as Van't Hoff Law [11], which is analogous to the ideal gas law and emerges out of purely entropic effects.

On the other hand, the  $\phi_p^2$  term is a measure of the two-body interactions, with its strength set by the coefficient  $A = 1/2 - \chi$ , where  $A$  is known as the virial coefficient [1].

Finally, as already mentioned in the previous section, for  $N \rightarrow \infty$  the entropic term becomes negligible and it's the two-body interaction effects that dominate, which gives us

$$\Pi \sim \phi_p^2 \quad (2.18)$$

For long polymer chains within the mean-field theory.

In the case of a polymer brush, experimental studies have shown [17] that the mean field theory gives the correct power law dependence of osmotic pressure on polymer volume fraction in the range where chains are not very long and the grafting densities moderate. For long chains in highly dense brushes, a better estimate of the power law is given by the scaling approach, which gives:

$$\Pi \sim \phi_p^{9/4} \quad (2.19)$$

Alternatively, the pressure can be obtained from kinematic instead of thermodynamic considerations. As will be derived in section 2.6.3, one can compute the local microscopic pressure tensor along the simulation box by taking both contributions from the momenta of the monomers (ideal gas contribution) and the forces due to the potentials acting on the monomers.

## 2.3 Evaluating Pressure in a Brush Bilayer

There are two different approaches to evaluating the osmotic pressure of a brush bilayer: the first is based on a global property of the system, the total free energy, and the second is based on an equation of state where the osmotic pressure is related to the minimum density in the brush profile. Both of these approaches will be discussed here.

### 2.3.1 Normal Pressure from the Free Energy

The first approach to getting the normal pressure of a brush bilayer is to consider the change in the total free energy as we're bringing the surfaces together: the isothermal work that goes into compressing the brushes results in an increase of the free energy of the system, and hence the osmotic pressure is given by [9]:

$$\Pi = \frac{\partial F}{\partial V} = \frac{1}{A} \frac{\partial F}{\partial D} \quad (2.20)$$

where  $F$  is the free energy of the system,  $A$  the area of the surfaces, and  $D$  their separation.

The earliest treatment of such a system is one where we consider two brushes separated by a distance  $2D$  with grafting density  $\sigma$  (Figure 2.6). To calculate the free energy of this system, we consider a simplified model [5] where all the chains have the same length  $N$  and the same height  $D$ . The volume per chain is then  $V = D/\sigma$ . Setting  $kT \equiv 1$  and  $b \equiv 1$  and using eq. 2.8, the free energy per unit area then becomes:

$$f = \sigma \frac{3D^2}{2N} + v \frac{(\sigma N)^2}{2D} \quad (2.21)$$

As before, the first term represents the stretching energy and the second term the

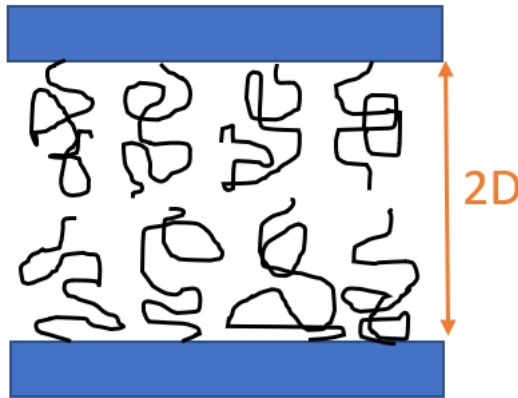


Figure 2.6: A Brush Bilayer

energy associated with the two-body interactions. The normal pressure (which,

as explained above, is the derivative of the free energy per unit area with respect to  $D$ ) is then given by:

$$\Pi = \frac{v}{2} \left( \frac{N\sigma}{H_0} \right)^2 \left[ \left( \frac{H_0}{D} \right)^2 - \frac{D}{H_0} \right] \quad (2.22)$$

Where  $H_0 = N(v\sigma/6)^{1/3}$  is the unperturbed brush height obtained after minimizing the free energy with respect to  $D$ .

However, such an approach does not account for the parabolic density profile of the brush due to the chain fluctuations of the chain ends along the height of the brush. A theory was therefore developed by Milner, Witten and Cates [18], in which they use the self-consistent field theory to obtain a free energy expression within the mean field approximation. The pressure obtained from that free energy is then given by:

$$\Pi = \frac{v}{2} \left( \frac{N\sigma}{H_0} \right)^2 \left[ \left( \frac{H_0}{D} \right)^2 - \frac{2D}{H_0} + \left( \frac{D}{H_0} \right)^4 \right] \quad (2.23)$$

With the prefactor and  $H_0$  being two adjustable parameters.

At strong enough compressions, the density profile along the normal direction to the surfaces becomes constant, given by  $\phi \approx N\sigma/D$ , which gives us an osmotic pressure of the form

$$\Pi \approx \frac{1}{2}v \left( \frac{\sigma N}{D} \right)^2 \quad (2.24)$$

It is important to note that this expression should be independent of polydispersity index [9].

### 2.3.2 Normal Pressure from the Equation of State

The second approach to evaluate the pressure is through the local density of the brush bilayer; since we're dealing with a system at equilibrium, the pressure along the normal direction must be uniform. Hence, it is enough to determine the pressure at one point (the minimum density in this case) to know the total normal pressure. In this system, there are two contributions to pressure: the positive contribution of the monomer-monomer interactions, and the negative contribution from the tension in the chains, due to their stretching away from their surface (which maximizes entropy and minimizes the free energy). This stretching can be characterized through the chemical potential  $\mu(z)$  of the chain, which must decrease as we move away from the surface (the farther we move away, the lower the probability of contact with another chain, and hence the lower the cost to place a chain at that point) [19]. Therefore, the grafted chains will tend



to stretch away from the surface along the gradient of the chemical potential, and at the minimum of the density where the gradient is zero, the stretching must disappear. The chains around the minimum must then behave as chains in a solvent, with the main contribution to pressure due to excluded volume effects only. The equation of state will then take the form:

$$\Pi(D) = \frac{1}{2}v\phi^2(D) \quad (2.25)$$

Where  $\Pi$  is the osmotic pressure of the system,  $v$  the virial coefficient (which should be equivalent to the excluded volume), and  $\phi(D)$  the density evaluated at the minimum in the  $z$  profile of the brush.

It was shown using SCF simulations [9] that these two characterizations of pressure were indeed equivalent, and that for strong enough compressions (when the density is uniform along  $z$ ) the pressure will depend on the local density only, and not on polydispersity index.

### 2.3.3 Interaction free Energy from Interbrush Contacts

A problem with the previous characterizations of free energy (section 2.3.1) was that they completely ignored the interpenetration of the two brushes upon compression, which would make the compressive force of purely entropic origin. However, as illustrated in figure 2.7, MD simulations and experiments clearly showed significant interpenetration [20]. This led to a new understanding of the compressive forces in a brush bilayer which helped develop a new approach to characterize the free energy of interaction (defined as the volume integral over the pressure due to compression [4]).

This approach is based on a line of reasoning whereby the contribution to the free energy inside the interpenetration zone is taken to be equal to that outside of it. The logic is as follows: if we compress the two brushes in a quasi-stationary process, the chains of opposite brushes will eventually start interpenetrating, establishing an interpenetration zone. The monomers of the opposite brushes in this zone will start repelling each other (interbrush interactions), which would lead to the compression of the grafted chains (intrabrush interactions) to avoid interpenetration. To maintain equilibrium, these two contributions must be balanced. Otherwise, the width of the interpenetration would not remain constant. Therefore, it is sufficient to compute the interaction free energy in the interpenetration zone to obtain the total interaction free energy (by multiplying by a factor of 2) [3]. A schematic extracted from that study can be seen in figure 2.8

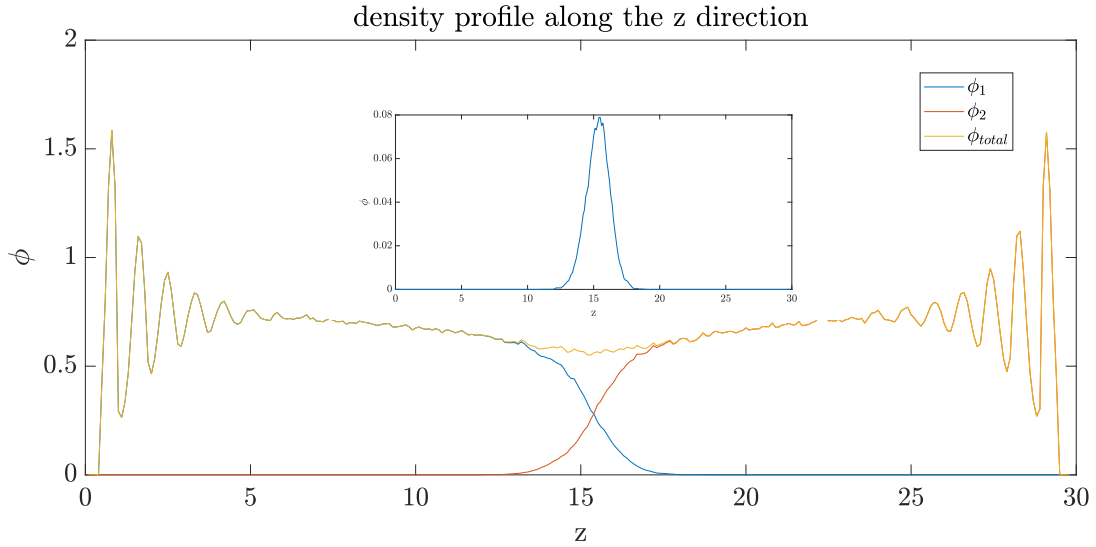


Figure 2.7: density profile of the brush bilayer system for  $k = 1.05$  at walls separation  $D = 30$ . The inset shows the overlap region, given by  $\Gamma = \phi_1\phi_2$  in which the brushes interpenetrate

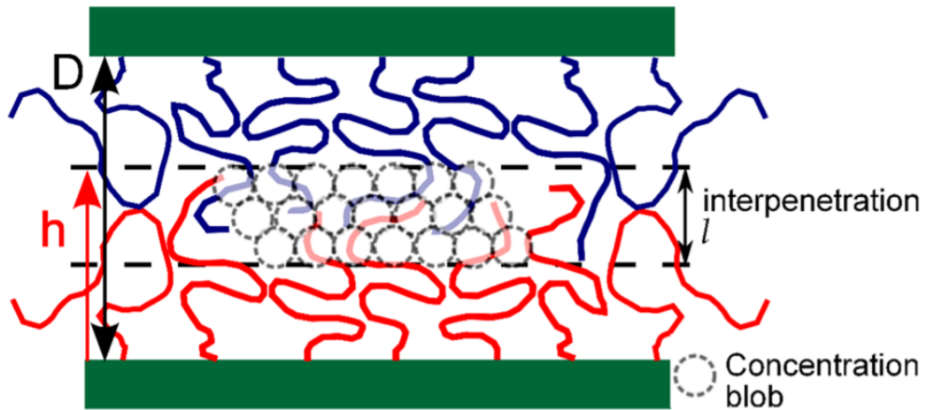


Figure 2.8: Schematic of a compressed polymer-brush bilayer. The free energy in the interpenetration zone of width  $l$  can be quantified through concentration blobs, each bringing energy of the order  $kT$  to the system.

This assumption was verified [3] by showing that the amount of interpenetration (quantified by the number of interbrush contacts) indeed followed the same functional form as the total interaction free energy (shifted by an arbitrary factor). However, this approach seems questionable; there is no solid footing over which we can claim that the number of interbrush contacts characterizes the total free energy of the system. Therefore, in our work, we attempt verify the consistency of this description by checking how the number of contacts relates to the

free energy of interaction, and checking if this description would be consistent over different polydispersity indices.

## 2.4 Modelling Chain Dynamics

### 2.4.1 The Dumbbell Model

At equilibrium, fluctuations in the position of monomers eventually lead to a change in the configuration of a polymer chain (figure 2.9). We can estimate how fast the configuration changes by adopting a bead-spring model [21]. For simplicity, we consider the Rouse model, where we ignore excluded volume and hydrodynamic interactions.

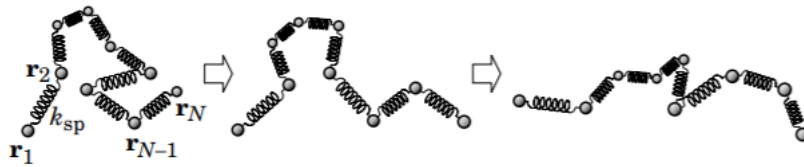


Figure 2.9: Change in the conformation of the chain in bead-spring model [1].

As in section 2.1.2, we consider a renormalized chain such that the orientation of each segment is independent of the other. Instead of considering these segments as rigid rods of Kuhn length  $b$ , we take them to be springs with equilibrium length  $b$ . The distance between two consecutive segments will then follow a Gaussian distribution  $P(\mathbf{R}) \sim \exp\left(-\frac{3\mathbf{R}^2}{2b^2}\right)$ . Similarly to eq.2.5, the stretching of the spring beyond its equilibrium length will lead to a restoring force with spring constant  $k = 3kT/b^2$  [1]. The elastic energy of the chain will then be the sum of the contributions from all subchains, which have the same form as eq.2.4. We can then write:

$$F = \sum_{n=0}^{N-1} \frac{3kT}{2b^2} \mathbf{r}_n^2$$

Since each bead will feel a force from both its neighbors (figure 2.10), the corresponding elastic force will be:

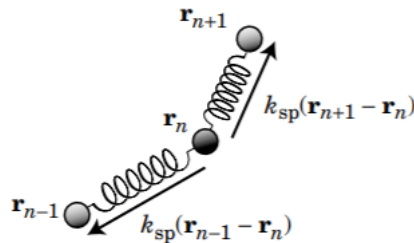


Figure 2.10: Spring force on bead  $n$  [1].

$$f_n = \partial F / \partial \mathbf{r}_n = \frac{3kT}{2b^2} (\mathbf{r}_{n+1} - 2\mathbf{r}_n + \mathbf{r}_{n-1}) \approx \frac{3kT}{2b^2} \frac{\partial^2 \mathbf{r}_n}{\partial n^2}$$

In addition to the elastic force, the beads will also be subject to random kicks from the surrounding solvent. The motion of that bead will then be governed by the Langevin equation [1]:

$$\xi \frac{d\mathbf{r}_n}{dt} = \frac{3kT}{2b^2} \frac{\partial^2 \mathbf{r}_n}{\partial n^2} + \mathbf{f}_n(t) \quad (2.26)$$

Where  $\xi$  is the drag coefficient and  $\mathbf{f}_n(t)$  the sum of random forces acting on the bead due to solvent molecules which satisfies

$$\begin{aligned} \langle \mathbf{f}_n(t) \rangle &= 0 \\ \langle f_n(t) f_n(t') \rangle &= 6kT\xi\delta(t-t') \end{aligned} \quad (2.27)$$

The Langevin equation can be easily solved if we represent the motion of the beads using normal coordinates  $\mathbf{q}_i$ . The dynamics are then described as the superposition of  $p$  independent normal modes. The solution obtained is then of the form [21]

$$\mathbf{r}_n(t) = \sum_p \alpha_p \cos\left(\frac{\pi p n}{N}\right) \exp\left(-\frac{t}{\tau_p}\right) \quad (2.28)$$

The zeroth normal mode  $p = 0$  represents the center-of-mass motion of the chain. The higher  $p$  is, the more sensitive to the local conformation the mode becomes, up to the  $N$ th mode which represents the motion of every monomer with respect to its neighbor. Each mode has its own relaxation time  $\tau_p = \tau_1/p^2$ , which is the characteristic time for  $N/p$  segments of the chain to diffuse through their end-to-end distance [21].

## 2.4.2 Properties of the Rouse Chains

Using eq.2.28, we can now obtain the two main quantities of interest to us: the diffusion coefficient for the polymer chain  $D_{chain}$  and the autocorrelation of the end-to-end vector  $\mathbf{R}(t) = \mathbf{r}_N(t) - \mathbf{r}_0(t)$ . For our purposes, we will write the final results without showing the calculations. The derivations can be found in ref. [1].

**Relaxation of the end-to-end vector** We first look at the time autocorrelation of the end-to-end vector. It can be shown that it's expressed as [1] :

$$\langle \mathbf{R}(t) \mathbf{R}(0) \rangle = \frac{8Nb^2}{\pi^2} \sum_{p:odd} \frac{1}{p^2} \exp(-tp^2/\tau_1) \quad (2.29)$$

We can see that the longest relaxation time  $\tau_1$  dominates the summation. Replacing  $\exp(-t/\tau_p)$  with  $\exp(-t/\tau_i)$  and using  $\sum_{p:\text{odd}} 1/p^2 = \pi^2/8$ , we finally obtain [1]

$$\langle \mathbf{R}(t)\mathbf{R}(0) \rangle \cong \langle \mathbf{R}^2 \rangle \exp(-t/\tau_1) \quad (2.30)$$

We find that in the Rouse model, the correlation of the end-to-end vector can be approximated by a single exponential. However, as we will show in a later section, this does not accurately describe the relaxation dynamics of a grafted chain in a polymer brush.

**Mean-square Displacement** We now turn to the fluctuations of a single bead. The diffusion coefficient of the chain can be obtained by considering its center-of-mass motion ( $p = 0$ ). A calculation of the mean-square displacement of the center of mass  $\mathbf{r}_{cm}$  (ref.[1]) gives:

$$\langle [\mathbf{r}_{cm}(t) - \mathbf{r}_{cm}(0)]^2 \rangle = 6 \frac{kT}{\xi N} t \quad (2.31)$$

We find that the displacement is similar to that of a Brownian particle  $\langle [r(t) - r(0)]^2 \rangle = 6Dt$ , with diffusion coefficient  $D_{chain} = \frac{kT}{\xi N}$ . We can see from this expression that the effective friction  $\xi_{eff} = \xi N$  is the sum of the  $N$  segment friction coefficients.

On the other hand, the mean-square displacement of a bead is given by[1]:

$$\langle [\mathbf{r}_n(t) - \mathbf{r}_n(0)]^2 \rangle = 6 \frac{kT}{\xi N} t + \frac{4Nb^2}{pi^2} \sum_p \cos^2 \left( \frac{\pi pn}{N} \right) \left[ 1 - \exp \left( -\frac{tp^2}{\tau_1} \right) \right]$$

If we take  $t$  to be larger than the longest relaxation time  $\tau_1$ , the first term in the equation dominates and the rms displacement of the bead is equal to that of the center-of-mass. At thermal equilibrium, one can take the reference  $\mathbf{r}(0)$  to be the average position  $\langle \mathbf{r} \rangle$ . We can finally write:

$$\langle \delta \mathbf{r}^2 \rangle = 6D_{chain} t \quad (2.32)$$

Where  $\delta \mathbf{r} = \mathbf{r}(t) - \langle \mathbf{r} \rangle$ .

From section 2.1.1, we know that  $\delta \mathbf{r}^2$  scales as  $N$ . Using eq. 2.32, we can finally obtain the scaling law of the Gaussian chain in the Rouse model, which is given by:

$$\tau \sim N^2 \quad (2.33)$$

One should note that while the Rouse model can only apply for polymer chains in the melt (where hydrodynamic interactions are screened), it was still used as the base model to describe the relaxation process of a monodisperse brush, as will be discussed in the next section.

## 2.5 Relaxation Dynamics of a Monodisperse Brush

### 2.5.1 Initial Description for Chain Relaxation

We now turn to study the dynamics of a polymer chain in a grafted monolayer. As we saw in the previous section (eq. 2.32), at thermal equilibrium, the motion of the overall chain can be reduced to that of a Brownian particle with diffusion coefficient  $D_{chain} = \xi N$ . For our current purposes, only the  $z$  component, taken to be perpendicular to the grafting surface is considered. The characteristic relaxation time  $\tau$  of its correlation function then goes as  $\tau \sim \langle \delta z^2 \rangle / D_{chain}$ .

In a grafted monolayer, analytical self-consistent field theory has shown that the mean square fluctuations of the chain end scale as  $\langle \delta z^2 \rangle \sim N^2$  [18], where  $N$  is the number of segments in a chain. We finally obtain the scaling law:

$$\tau_{\perp} \sim N^3 \quad (2.34)$$

These fluctuations along the height of the chain are anomalously large ( $\delta z \sim N$  instead of  $N^{1/2}$  as is the case of a Gaussian chain). This was shown to be evidence of the polymer chains being near a coil-stretch phase transition (Figure 2.11) which results in a critical slowing down in the relaxation times of the chains [5].

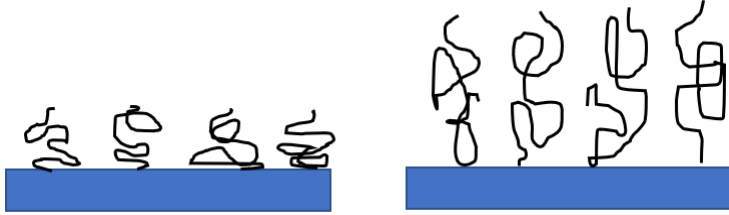


Figure 2.11: Brush in the coil regime (left) and in the stretched regime (right)

However, these anomalous fluctuations occur only along the  $z$  component of the chain. Along the lateral components, it was found that the relaxation times are compatible with the Rouse model [22]:

$$\tau_{\parallel} \sim N^2 \quad (2.35)$$

Finally, one should note that in this model, there are no entanglement effects and the scaling of relaxation times with  $N$  was found to be independent of grafting density and solvent quality [5].

### 2.5.2 Later Discoveries and Modifications

We now consider the normalized autocorrelation function of the end-to-end vector

$$\phi_{\mathbf{R}}(t) = \frac{\langle (\mathbf{R}(t) - \langle \mathbf{R} \rangle)(\mathbf{R}(0) - \langle \mathbf{R} \rangle) \rangle}{\langle \mathbf{R}^2 \rangle - \langle \mathbf{R} \rangle^2} \quad (2.36)$$

We already saw in the context of the Rouse model (eq.2.29) that the autocorrelation function decays in a spectrum of correlation times, but is dominated by the slowest time  $\tau_1$ . The decay was then approximated by an exponential with an effective characteristic time  $\tau_{eff} \approx \tau_1$ .

However, a more recent study showed that  $\phi_{\mathbf{R}}(t)$  is strongly curved at the beginning, so this approximation was not in fact valid, except for small values of the autocorrelation function ( $\phi_{\mathbf{R}} < 0.1$ ) [8]. This problem only became obvious after conducting Molecular Dynamics (MD) instead of Monte Carlo simulations where the data was only available in the regime  $\phi_{\mathbf{R}}(t) > 0.2$ .

In this study, another surprising result was found: while the relaxation time of the center of mass behaved as expected in the context of the Rouse model, ( $\tau_{\perp} \sim N^3$  and  $\tau_{\parallel} \sim N^2$ ), the relaxation of the end-to-end vector was not so obvious; it was shown that the relaxation of the parallel and perpendicular components obeys an empirical power law  $\tau \sim N^{\Delta}$ , with  $\Delta$  having the same value for *both* the parallel and perpendicular components [8] such that:

$$\begin{aligned} \tau_{\perp} \sim \tau_{\parallel} &\sim N^3 && \text{For } N < 64 \\ \tau_{\perp} \sim \tau_{\parallel} &\sim N^{3.7} && \text{For } N \geq 64 \end{aligned} \tag{2.37}$$

A possible interpretation of this behavior was given by considering the anisotropy in the Brownian motion of a chain. In previous models, it was assumed that the fluctuations in this motion in the  $z$ -direction was independent of those in the  $xy$ -directions. In that case, following eq.2.32, we could estimate the effective friction coefficient from

$$\xi_{eff} = \tau_i / N \langle \delta r_i^2 \rangle \tag{2.38}$$

Where  $i = x, y, z$ . Additionally, because we're not in the completely stretched regime, one would expect the friction coefficient to be isotropic (there is not stretching effect on length scales smaller than the blob). We therefore expect that  $\xi_{eff}$  would converge to a plateau value for all  $i$ .

It was shown, however, that these predictions were only valid in the earlier stages of the relaxation ( $\phi(t) > 0.2$ ) [8]. In the later stages, the value of  $\xi_{eff}$  given by the definition above significantly increases, and becomes strongly anisotropic with large  $N$ , which makes this characterization of the friction coefficient invalid. The authors then concluded that in the later stages of the relaxation, the fluctuations in the lateral and perpendicular motion of the chain cannot be decoupled as was assumed before. Instead, the relaxation becomes controlled by the slowest relaxing component (in this case, the lateral components). Therefore, we can no longer assume a proportional relation between the relaxation times and the mean square fluctuations as in eq.2.32.

However, whether this coupling is present in the case of a polydisperse brush (where chains are not of equal length) is still an open question; It was shown



[2] that even in the case of small polydispersity, the end of the chains fluctuates around its mean position, as opposed to fluctuating along the height of the brush in the monodisperse case. The anomalous fluctuations are then suppressed with increasing polydispersity.

In this work, we will therefore investigate the relaxation properties of such a system and check for an apparent coupling in the fluctuations. In the next section, we explain the model used to generate our polydisperse brush.

## 2.6 Models and Methods

For our purposes, we conduct coarse-grained molecular dynamics (MD) simulations using both C as a programming language and the python library HOOMD-blue.

We model a flexible chain in a good solvent where monomers tend to repel each other. We can then account for the solvent implicitly by setting the interactions between monomers to be purely repulsive. Additionally, random collisions with the solvent are accounted for by including both a friction term and a random force. Therefore, the Langevin equations were the most appropriate for our model (see section 2.6.1).

### 2.6.1 The Model

The setting up and initial equilibration of the brushes was done through the python library HOOMD-blue, which runs the simulations on GPU. For simplicity, the monomers are initially set up to be stretched upwards in a lattice positioning and then left to equilibrate. The dimensions of the simulation box were taken to be  $L_x = L_y = N\sigma_d$  where  $N$  is the number of grafted monomers along the  $xy$  directions and  $\sigma_d$  is the grafting distance. Repulsive grafting surfaces were placed on  $L_z = 0$  and  $L_z = 2L_{max}$ , where  $L_{max}$  is the length of the completely stretched chains. Periodic boundary conditions were used in the lateral directions. To model hardcore repulsion between two monomers, the WCA potential (truncated and shifted Lennard-Jones potential) was used such that:

$$U_{WCA}(r) = \begin{cases} 4\epsilon [(\sigma/r)^{12} - (\sigma/r)^6] + \epsilon & r \leq 2^{1/6}\sigma \\ 0 & \text{otherwise} \end{cases} \quad (2.39)$$

Where  $\epsilon$  is the upward shift in the potential and the cut-off  $2^{1/6}\sigma$  is the potential minimum of the Lennard-Jones potential. As for the bonded monomer interactions along the chain (nearest neighbours), the Kremer-Grest potential was used. It is a bead-spring model where the repulsion between the neighbouring monomers is modelled through the WCA potential, and the bonded interactions modelled by the finite extensible nonlinear spring (FENE) potential given by:

$$U_{FENE}(r) = -\frac{kR^2}{2} \ln \left[ 1 - \left( \frac{r}{R} \right)^2 \right] \quad (2.40)$$

Where  $R = 1.5\sigma$  and  $k = 30\epsilon\sigma^{-2}$ . The interactions with the wall were modelled through a strongly repulsive potential given by:

$$U_{WALL}(z) = \epsilon \left( \frac{\sigma}{z} \right)^{12} + Az + B \quad (2.41)$$

Where  $A$  and  $B$  were both chosen such that both the potential and its derivative (force) vanish at  $z = \sigma/2$ .

The forward integration in time is driven by the Langevin equations such that:

$$m \frac{d\mathbf{v}}{dt} = \mathbf{f}_c - \gamma \cdot \mathbf{v} + \zeta(t) \quad (2.42)$$

Where we take our units such that the mass of a monomer  $m = 1$ .  $\mathbf{f}_c$  is the net force on the particle from all the potentials (WCA and FENE),  $\mathbf{v}$  the particle velocity,  $\gamma = 0.25$  the drag coefficient and  $\zeta(t)$  the random force due to the density fluctuations in the solvent (with magnitude consistent with the fluctuation-dissipation theorem), with properties

$$\begin{aligned} \langle \zeta(t) \rangle &= 0 \\ \langle |\zeta(t)|^2 \rangle &= 6kT\gamma/\delta t \end{aligned} \quad (2.43)$$

Computing equilibrium properties (microscopic pressure tensor, energy of brush-brush interactions, relaxation times...) was done through a MD program on C that uses the same setup. The integration of the equations of motions was done through the Verlet algorithm. The implementation of polydispersity and the computation of the pressure are explained in detail in the next sections. Computing the pressure tensor was implemented following the method described in section 2.6.3.

## 2.6.2 Model of a Polydisperse Brush

To implement polydispersity, we use the Schulz-Zimm (SZ) distribution for the chain length distribution [23][24] given by

$$P(N) = \frac{k^k N^{k-1}}{\Gamma(k) N_n^k} \quad (2.44)$$

Where the number-averaged chain length  $N_n$ , as well as the parameter  $k$  (related to the index of polydispersity) are free parameters.  $\Gamma(k)$  is the Gamma function. The first-order moment is given by  $\int_0^\infty dN N P(N) = N_n$ , and the higher order moments can be recovered from the recursion formula  $\langle N^m \rangle = \langle N^{m-1} \rangle N_n \frac{k+m-1}{k}$

The distribution of polymer chains can be characterized by the weight distribution, given by

$$P_w(N) = \frac{N P_n(N)}{\sum_0^\infty N P_N(N)} = \frac{N P_n(N)}{\langle N \rangle}$$

The mean of this distribution is then the weight-averaged chain length, given by [11]

$$N_w = \frac{1}{\langle N \rangle} \sum_0^\infty N P_w(N) = \frac{1}{\langle N \rangle} \sum_0^\infty N^2 P_n(N) = \frac{\langle N^2 \rangle}{\langle N \rangle} = N_n \frac{k+1}{k}$$

We define the polydispersity index as the ratio between the weighted average length and the average length:

$$\frac{N_w}{N_n} = 1 + \frac{1}{k} \quad (2.45)$$

As  $k \rightarrow \infty$ ,  $N_w/N_n \rightarrow 1$  and the distribution is monodisperse. Figure 2.12 shows the probability distribution of chain lengths for different polydispersity indices.

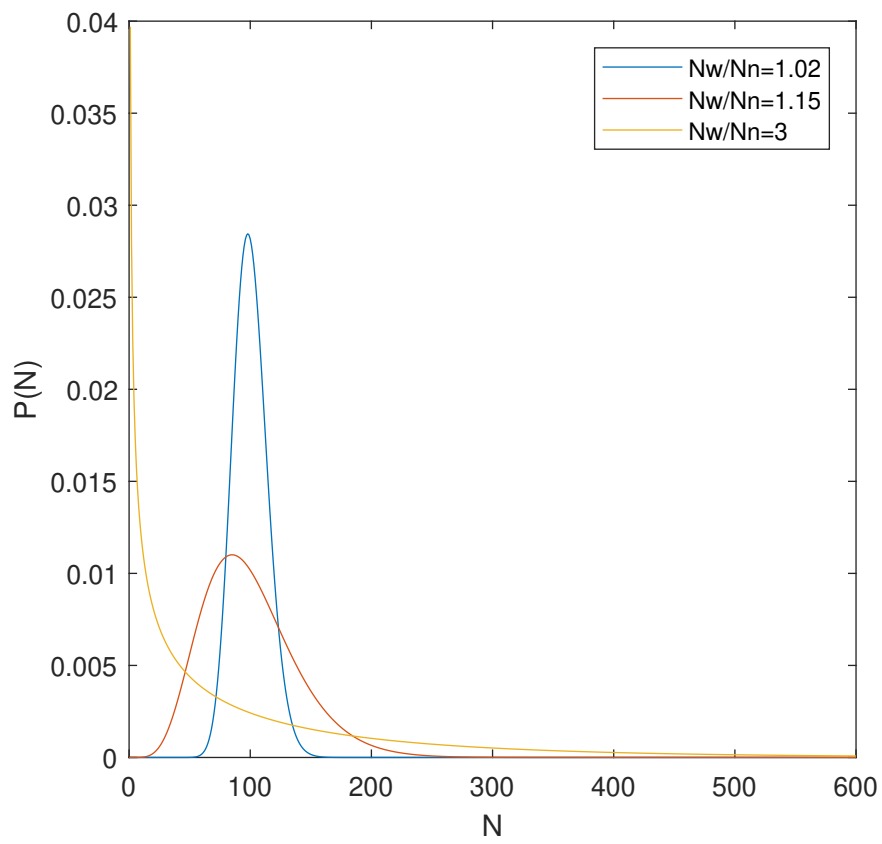


Figure 2.12: Schulz-Zimm distribution for  $N_n = 100$  and  $N_w/N_n = 1.02, 1.15, 3$ .

### 2.6.3 Microscopic Pressure Tensor

Here we derive the expression and explain the model used to compute the microscopic pressure tensor.

At the microscopic level, for a system of  $N$  point particles, the force is defined as the rate of change of linear momentum within a volume  $V$ . The total linear momentum is

$$\mathbf{P}_V(t) = \int_V d^3\mathbf{R} \mathbf{J}(\mathbf{R}, t) \quad (2.46)$$

Where  $\mathbf{J}(\mathbf{R}, t) = \sum_i \mathbf{p}_i(t) \delta[\mathbf{R} - \mathbf{r}_i(t)]$  is the momentum density. Differentiating with respect to time and using  $\nabla_{\mathbf{r}_i}^\beta f(\mathbf{R} - \mathbf{r}_i) = -\nabla_{\mathbf{R}}^\beta f(\mathbf{R} - \mathbf{r}_i)$ , one obtains [25]

$$\begin{aligned} \mathbf{J}^\alpha(\mathbf{R}, t) &= -\nabla_{\mathbf{R}}^\beta \sum_i p_i^\alpha \dot{r}_i^\beta \delta(\mathbf{R} - \mathbf{r}_i) + \sum_i \dot{p}_i^\alpha \delta(\mathbf{R} - \mathbf{r}_i) \\ &= -\nabla_{\mathbf{R}}^\beta \sum_i \frac{p_i^\alpha p_i^\beta}{m} \delta(\mathbf{R} - \mathbf{r}_i) - \sum_i \nabla_i^\alpha \Phi(\{\mathbf{r}_i\}) \delta(\mathbf{R} - \mathbf{r}_i) \end{aligned} \quad (2.47)$$

Where  $\alpha, \beta = x, y, z$ , and  $\Phi(\{\mathbf{r}_i\})$  is the total potential in the absence of external fields.

The first term is the kinetic part of the pressure tensor, due to particles entering and leaving the volume  $V$ . The second is the interaction part, which is comprised of all pair interactions. Using the translational invariance of the inter-particle potential, the potential could be re-expressed as the gradient of the line integral starting at an arbitrary point  $\mathbf{R}_0$  and ending at  $\mathbf{r}_i$  [25]

$$\nabla_i^\alpha \Phi(\{\mathbf{r}_i\}) \delta(\mathbf{R} - \mathbf{r}_i) = -\nabla_{\mathbf{R}}^\beta \sum_i [\nabla_i^\alpha \Phi(\{\mathbf{r}_i\})] \oint_{C_{0i}} dl^\beta \delta(\mathbf{R} - \mathbf{l}) \quad (2.48)$$

Where  $C_{0i}$  is any contour from an arbitrary point  $\mathbf{R}_0$  to  $\mathbf{r}_i$ . For pair interactions, the potential is of the form

$$\Phi(\{\mathbf{r}_i\}) = \sum_{i,j} \phi(r_{ij}) \quad (2.49)$$

Where  $r_{ij} = |\mathbf{r}_j - \mathbf{r}_i|$ . It is convenient to simply take  $C_{0i}$  to be the line between  $\mathbf{r}_i$  and  $\mathbf{r}_j$ .

As illustrated in figure 2.13, the energy of interaction between  $\mathbf{r}_i$  and  $\mathbf{r}_j$  will contribute a certain fraction  $\lambda_i$  of its total energy to each volume element in our system. We then write:

$$\begin{aligned} \mathbf{l} &= \mathbf{r}_i + \lambda(\mathbf{r}_j - \mathbf{r}_i), \quad \lambda \in [0, 1] \\ d\mathbf{l} &= d\lambda(\mathbf{r}_j - \mathbf{r}_i) \end{aligned} \quad (2.50)$$

This is known as the Irving and Kirkwood choice of integration contour [26].

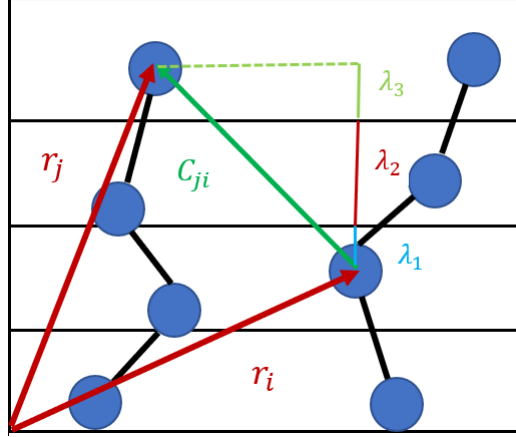


Figure 2.13: The Irving-Kirkwood contour. In each slice, the interaction force contributes a fraction  $\lambda_i$  to the configurational part of the stress tensor

Using eq. 2.49 and eq. 2.50, we can write eq. 2.48 as

$$\begin{aligned} \nabla_i^\alpha \Phi(\{\mathbf{r}_i\}) \delta(\mathbf{R} - \mathbf{r}_i) &= -\nabla_{\mathbf{R}}^\beta \sum_{i,j} \phi'(r_{ij}) \frac{r_{ij}^\alpha}{r_{ij}} \oint_{C_{ij}} d\mathbf{l}^\beta \delta(\mathbf{R} - \mathbf{l}) \\ &= -\nabla_{\mathbf{R}}^\beta \sum_{i,j} \phi'(r_{ij}) \frac{r_{ij}^\alpha}{r_{ij}} r_{ij}^\beta \int_{C_{ij}} d\lambda \delta(\mathbf{R} - \mathbf{r}_i + \lambda(\mathbf{r}_{ij})) \end{aligned} \quad (2.51)$$

Substituting (2.7) in (2.3), the change in momentum density becomes

$$\mathbf{J}^\alpha(\mathbf{R}, t) = -\nabla_{\mathbf{R}}^\beta \left[ \sum_i \frac{p_i^\alpha p_i^\beta}{m} \delta(\mathbf{R} - \mathbf{r}_i) + \sum_{i,j} \phi'(r_{ij}) \frac{r_{ij}^\alpha}{r_{ij}} r_{ij}^\beta \int_{C_{ij}} d\lambda \delta(\mathbf{R} - \mathbf{r}_i + \lambda(\mathbf{r}_{ij})) \right] \quad (2.52)$$

The quantity in brackets is the stress tensor  $\sigma^{\alpha\beta}$ , which, as mentioned, is the sum of both kinetic and configurational contributions. We define the pressure tensor as the ensemble average over all configurations of the stress tensor. Setting  $\phi' = -f_{ij}$ , where  $f_{ij}$  is the interaction force between particles  $i$  and  $j$ , the expression for the pressure tensor becomes

$$\begin{aligned} \mathbf{P}(\mathbf{R}) &= \frac{1}{V} \int \left[ \sum_i \frac{p_i^\alpha p_i^\beta}{m} \delta(\mathbf{R} - \mathbf{r}_i) - \sum_{i,j} f_{ij} \frac{r_{ij}^\alpha}{r_{ij}} r_{ij}^\beta \int_{C_{ij}} d\lambda \delta(\mathbf{R} - \mathbf{r}_i + \lambda(\mathbf{r}_{ij})) \right] d\mathbf{R}^3 \\ &= \frac{1}{V} \sum_i \frac{p_i^\alpha p_i^\beta}{m} - \frac{1}{V} \sum_{i,j} f_{ij} \frac{r_{ij}^\alpha}{r_{ij}} r_{ij}^\beta \int_{C_{ij}} d\lambda \end{aligned} \quad (2.53)$$

This equation will be implemented on the brush bilayer system to evaluate the local pressure along the surface perpendicular to the grafting density.

# Chapter 3

## Results

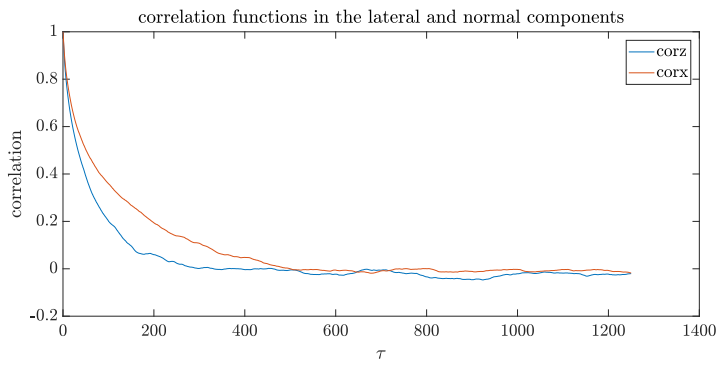
### 3.1 Relaxation times

#### 3.1.1 Monodisperse Brush

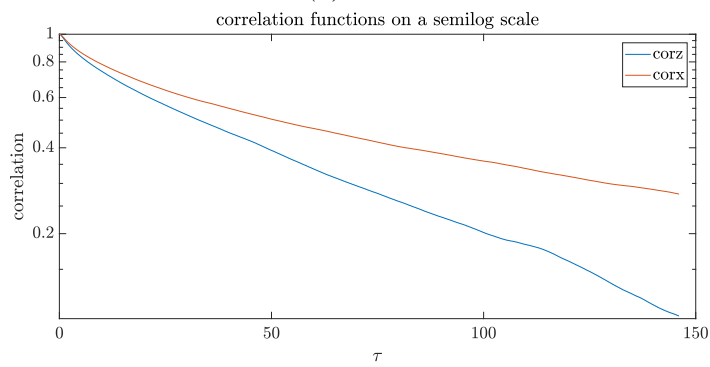
As a check of our setup, we start by computing the relaxation times and fluctuations in a monodisperse polymer brush. We consider a system of 25 chains of  $N = 10, 15, 20, 25$  monomers, grafted with a density of  $\sigma_g = 0.1$  chains per unit area, with our unit length being  $\sigma = 1$ . We initially set up the chains to be completely stretched in the  $z$  direction, and let equilibrate for  $1e6$  MD steps. Afterwards, we further run for  $1e7$  steps while recording the  $z$  and  $x$  components of the end-to-end vector of each chain. The data was processed on Matlab using the autocorr function. It is important to note that autocorr gives reliable results only if the number of time intervals  $\tau$  (over which the correlations decay) is less than a fourth of the number of frames in our data (snapshots of the positions of the end-to-end vectors). A sample of the correlation functions can be seen in figure 3.1a. Figure 3.3 shows the density profile of a monodisperse brush, which indeed has the predicted parabolic shape, except for the tail at the end due to fluctuations and the ordering near  $z = 0$  due to wall effects (these effects cannot be accounted for in the context of the mean field theory).

To extract the relaxation times, we plot the correlation functions on a semilog scale and fit the linear portion (disregarding the initial quick relaxation of the higher modes) (see figure 3.1b). The relaxation time  $\tau$  is then simply the inverse of the slope obtained from the fit.

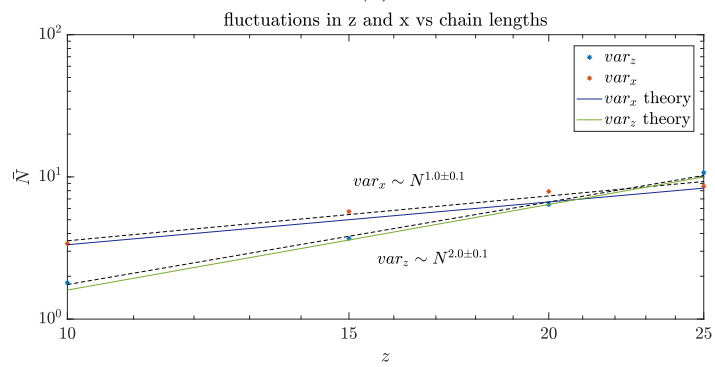




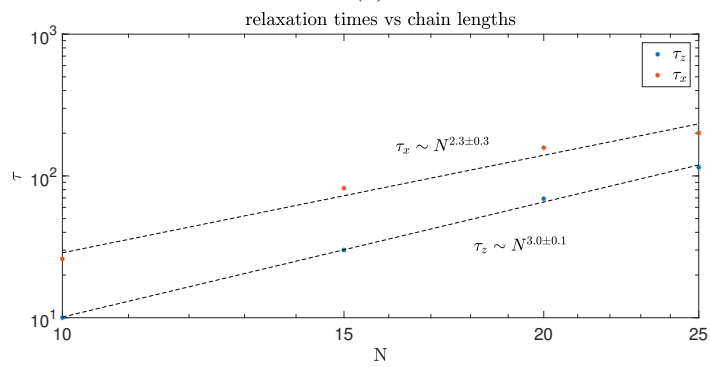
(a)



(b)



(c)



(d)

Figure 3.2: 3.1a shows correlation functions in  $x$  and  $z$  vs the time intervals  $\tau$  (in natural units). Figure 3.1c shows the fluctuations in  $x$  and  $z$  vs the number of monomers per chain  $N$  on a loglog scale. The dashed lines represent the linear fits from which a slope of 2.0 was extracted for the  $z$  component and 1.0 for the  $x$  component, in accordance with the Rouse model. The solid lines represent the theoretical curves for the fluctuations in  $x$  and  $z$ . Figure 3.1d shows the relaxation times in  $x$  and  $z$  vs  $N$ , with linear fits (dashed lines) for the  $z$ -component from which a slope of  $3.0 \pm 0.1$  was obtained, and a slope of  $2.3 \pm 0.3$  for the  $x$ -component. These power laws are also consistent with those predicted by the Rouse model ( $\tau_z \sim N^3$  and  $\tau_x \sim N^2$ )

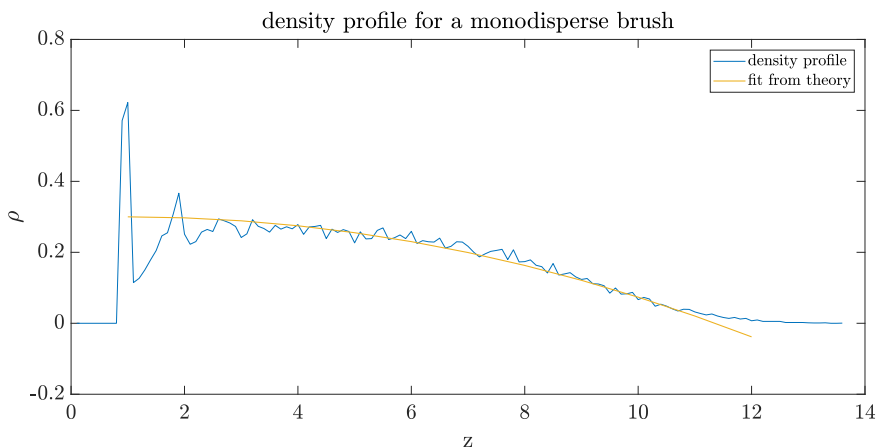


Figure 3.3: Average density profile of a monodisperse brush with  $n_c = 25$  and  $N_n = 20$  along  $z$ . The binning was done along slices of width  $0.1\sigma$ . The fit is obtained from the analytical form, where we set  $v = 3.6$  and  $\sigma = 1/9$

The obtained scaling laws are shown in figures 3.1c and 3.1d. We find that the scaling law of both the correlations and the fluctuations followed our predictions within the framework of the Rouse model: the relaxation time in  $z$  scaled as  $\tau_z \sim N^3$  and in  $x$  as  $\tau_x \sim N^2$ , while the fluctuations scaled as  $\langle \delta z^2 \rangle \sim N^2$  in  $z$  and  $\langle \delta x^2 \rangle \sim N$  in  $x$  (within the statistical uncertainty). Additionally, we compare our data to theoretical curves, given by  $var_x = N/3$  and  $var_z = 0.016 * N^2$ . The form of  $var_z$  was obtained from fitting the density profile (see figure 3.3) into the analytical form  $\rho(z) = \rho_0(1 - z^2/H_{mono}^2)$  [2]. The fluctuations are then  $var_z = (2/5 - (3\pi/16)^2)H_{mono}^2$ . We find that our data matches fairly well with the theoretical predictions.

These results are evidence that the late relaxation dynamics in long chains due to the coupling between the lateral and normal degrees of freedom is not apparent in the regime of short chains, which implies that there is little to no entanglement in the regime we're considering (for the polydisperse brushes as well).

### 3.1.2 Polydisperse Brush

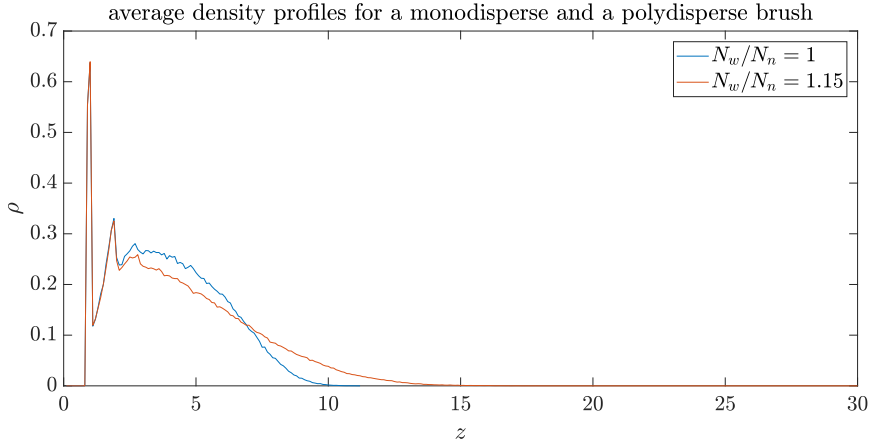
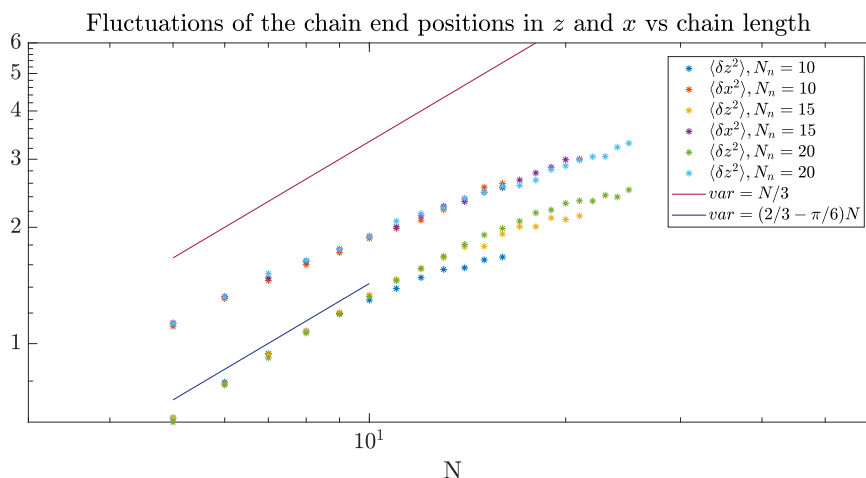
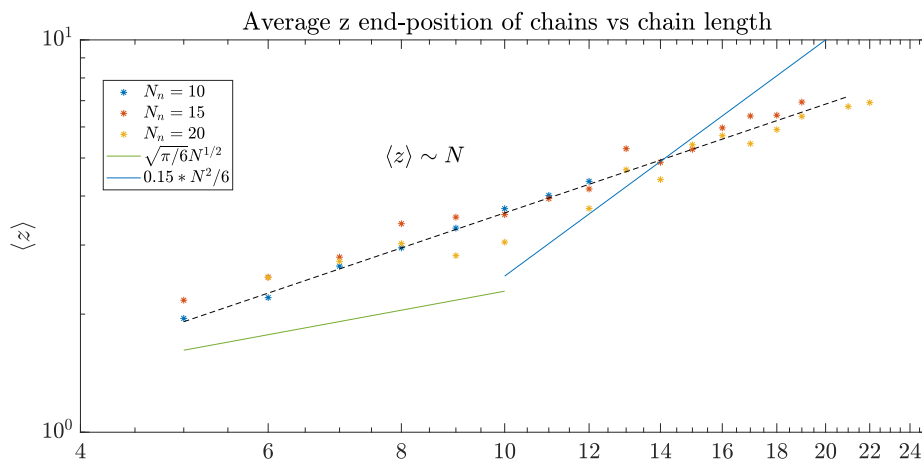


Figure 3.4: Average density profile of a monodisperse (blue) and polydisperse (red) brush with  $n_c = 25$  and  $N_n = 15$  along  $z$ . The binning was done along slices of width  $0.1\sigma$

We can now move on to study the effects of polydispersity on the relaxation times. We set up a system of  $n_c = 49$  chains per brush. The length of each chain is randomly sampled from the Schulz-Zimm distribution (see section 2.6.2), with  $N_w/N_n = 1.15$  and  $N_n = 10, 15, 20$ . This polydispersity index was chosen because it results in an approximately linear density profile. The starting configuration and equilibration were performed as with the monodisperse case, then trajectories were run for  $1e7$  steps while recording the  $z$  and  $x$  components of the end-to-end vector of each chain to generate the correlation functions. This procedure was repeated with 20 different samples of brushes with randomly distributed chain lengths, and our final correlation function is averaged over all the samples. As was mentioned in section 2.5, we expected that in a polydisperse brush, the linear density profile (figure 3.4) will generate a mean field that would stretch the chain away from the grafting surface in such a way that the end monomers would exhibit gaussian fluctuations (in contrast with the monodisperse brush with the parabolic profile under which chain ends fluctuate along the entire height of the brush). Unless there are some unknown late relaxation processes due to possible entanglement effects, these thermal fluctuations are expected then to restore the  $\tau_z \sim N^2$  power law dependence on  $N$  of the relaxation times. The results we actually got were not only unexpected, but also very unclear with no obvious interpretation;



(a) chain end fluctuations in  $x$  and  $z$  vs chain length  $N$  for  $N_n = 10, 15, 20$ . The theoretical curve for gaussian fluctuations are shown in red, and the theoretical curve for fluctuations in the presence of a wall in blue.



(b) dependence of the mean  $z$  position of the chain end vs  $N$ . The theoretical prediction for the mean positions in the presence of the wall is shown in green, and that of the SCF theory in blue. Neither matched our predictions. Our fit (which gave a slope of  $1 \pm 0.2$  is shown as the dotted line.)

Figure 3.5: mean positions and fluctuations of chain ends

Indeed, looking at the fluctuations of the position of the end monomers (figure 3.5a), we find two unexpected behaviors: first of all, the fluctuations in  $x$ , which were supposed to be Gaussian as in the monodisperse case, strongly deviate from the predicted behavior ( $var = N/3$ ). We find that the theoretical curve is shifted upwards by a factor of at least 3, and that our fluctuations vary less strongly with  $N$ . This remains yet to be explained, and requires further study beyond the scope of this thesis.

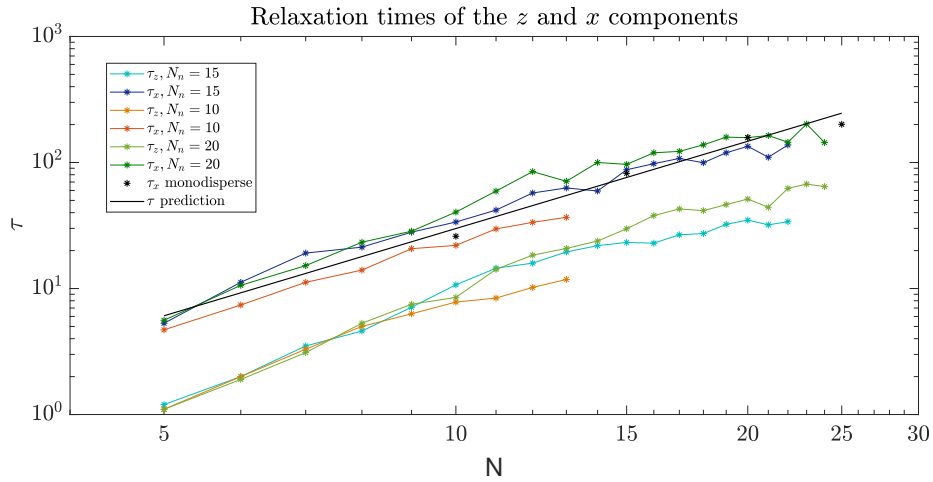
Second, we find that the fluctuations in  $z$  display two regimes: in the range

$N < 10$ , the fluctuations increase linearly with  $N$ , and do not change with number average  $N_n$ . This behaviour can be attributed to wall effects, as we find that the theoretical curve ( $var = (2/3 - \pi/6)N$ ) does match with our data (besides a small shift of about 0.8%). However, for  $N > 10$ , the fluctuations show a systematic reduction and start depending on  $N_n$ . This behavior has no clear interpretation. One idea might be that for the longer chains in our sample, the field becomes inhomogeneous because of polydispersity. We cannot then expect gaussian fluctuations, which can only happen in homogeneous fields. However, to confirm this hypothesis, more studies should be conducted which will be left for future work.

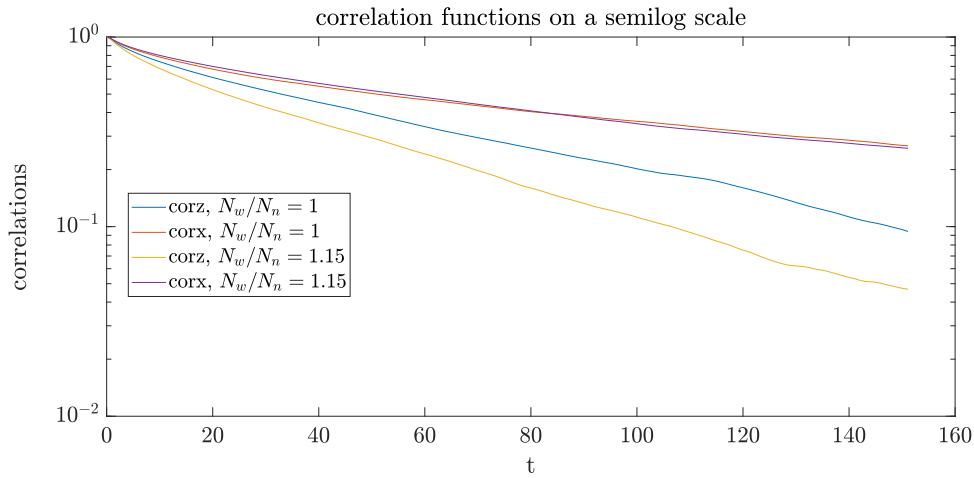
Moreover, looking at the mean positions of chain ends (figure 3.5b), we find that its dependence on  $N$  does not match with any framework we know of, which implies that the theory might not be representative of the actual behavior of the polydisperse brush.

Moreover, we look at the dependence of the relaxation times on  $N$  (figure 3.6a), and find the behavior consistent with that of the fluctuations: the relaxation times in  $z$  are reduced for  $N > 10$ , and depend significantly on the number average. As for the  $x$  component, we surprisingly find that although the fluctuations were much smaller than in the monodisperse case, the relaxation times matched those of the monodisperse brush, which also remains puzzling. As can be seen in figure 3.6b, the relaxation time in  $z$  is significantly smaller for a polydisperse brush than that of a monodisperse (which makes sense, considering the fluctuations are about 3 times smaller), but match very well in the  $x$  direction. Finally, it should be noted that  $\tau$  monodisperse in figure 3.6a, which was obtained from fitting our data for  $\tau_x$  in a monodisperse brush, was predicted to match not only our data in  $x$ , but also in  $z$  (since we were supposed to recover gaussian fluctuations in all directions). One possible explanation for these deviations from theory, as hinted before, could be related to the anisotropy in the field a single chain is subject to: due to the polydispersity in our system, a chain of the same length could be subject to different potentials depending on the sample we're considering, which would most likely affect its dynamics and therefore its relaxation. This would explain the discrepancies we see with different number averages: the fields are likely uniform for short chains, but once the chain becomes long enough, the configuration space it explores would start varying depending on the system.

As attempting to explore the entirety of the configuration space proved to be too resource-demanding, we decided not to pursue things further and leaving the matter for future studies. However, one thing we can extract from our data is the time scale over which the chains in a brush relax: the highest relaxation times obtained were of the order of 100 in natural units (around 200,000 MD steps). This provided us with a scale over which to run our trajectories in our brush-bilayer system in the next part of the thesis work, where we ran things for trajectories of the order of  $1e7$  steps.



(a) relaxation times vs chain length  $N$  for different number averages for  $N_w/N_n = 1.15$ . The data previously obtained for the monodisperse case is also shown, along with a fit of this data (solid black line).



(b) correlation functions on a semilog scale for  $N_w/N_n = 1$  and  $N_w/N_n = 1.05$

Figure 3.6: figure 3.1a shows the relaxation times for  $N_w/N_n = 1.15$ ,  $N_n = 10, 15, 20$

## 3.2 Pressure and Interaction Free Energy

### 3.2.1 Equation of state of a WCA gas

As a first check to our pressure tensor algorithm (described in the methods section), we start by reproducing the well-established equation of state of a gas formed by purely repulsive monomers (interacting through a WCA potential) [27]. The equation of state is given by:

$$P = nk_B T + P_{WCA}$$

Where  $P$  is the total pressure of the system,  $n$  the density of monomers,  $k_B$  the Boltzmann constant and  $T$  the temperature. We set  $k_B = T = 1$ .  $P_{WCA}$  is the non-ideal contribution to the pressure, and is given by:

$$P_{WCA} = nk_B T \left( \frac{nB^{WCA}}{(1 - v_{eff})^2} + 2 \frac{(nv_{eff})^2}{(1 - nv_{eff})^3} \right) \quad (3.1)$$

The virial coefficient  $B^{WCA} \approx 2.2$  can be obtained by evaluating eq. 2.6 with  $U(r) = U_{WCA}(r)$ , where  $U_{WCA}$  is given by eq 2.39, and the temperature-dependent effective volume is evaluated from  $v_{eff}(T) = (\pi/6)d_{eff}^3$ , where  $d_{eff}$  is defined as the separation between monomers over which their interaction potential is equal to  $k_B T$ . For temperature  $T = 1$ , we obtain  $v_{eff} = 0.5$ .

To evaluate the pressure in our system, we run MD simulations (using the velocity verlet algorithm described in the methods section). We set up a cubic simulation box with side lengths  $L = L_x = L_y = L_z$  varying from  $L = 19$  to  $L = 6$ . We implement periodic boundary conditions in all directions. Our system consists of  $N = 500$  monomers interacting through the WCA potential. We initially place these monomers in a lattice position, separated by a distance equal to  $\sigma = 1$ , where our unit length  $\sigma$  is the finite distance at which the inter-particle Lennard-Jones potential is zero. We let the system initially relax for  $5e6$  MD steps, with integration step  $dt = 5e - 4$ . We then decrease the side lengths of the box at increments of  $0.1\sigma$ , and equilibrate for an additional  $5e6$  MD steps at each increment. At each increment of 1, we run our simulations for an additional  $5e6$  steps, but this time while evaluating the density and the components the pressure tensor every 500 steps. We therefore obtain  $1e4$  "snapshots" to average over. The final result can be shown in figure 3.7:

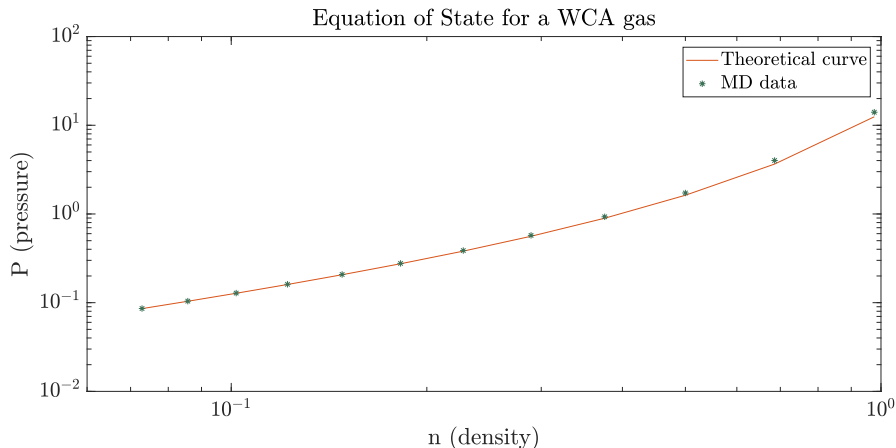


Figure 3.7: *log-log plot of the total pressure vs monomer density for a gas of  $N = 500$  monomers interacting through a WCA potential*

We find that our data extracted from the simulations fits perfectly with the theoretical curve, from which we can conclude that our implementation of the microscopic pressure tensor is reliable.

### 3.2.2 Compressing a Monodisperse Brush Bilayer

Next, we proceed to set up our brush bilayer, where we place two opposing grafting surfaces separated by a distance  $D$ . We define the  $z$ -axis to be the direction normal to these two surfaces. The lower surface is at  $z = 0$  and the upper one at  $z = D$ . Our system consists of  $n_c = 25$  chains of  $N = 20$  monomers on each grafting surface. The chains were grafted at a density  $\sigma_g = 0.5$ . The simulation box dimensions were  $L_x = L_y = \sigma_d \sqrt{n_c}$  and  $Lz = D$ . Periodic boundary conditions were applied in the lateral directions (along the  $xy$ -axes). More details can be found in the models and methods section.

For time efficiency, the setup, relaxation, and compression of the system was conducted using the python library HOOMD-blue, which makes use of the GPU. However, as it was not possible to directly calculate the local pressure tensor (there were no such functions available), nor was it possible to resolve the individual forces contributions on each monomer, the collection of data was conducted using our implemented microscopic pressure tensor algorithm on C.

As with the WCA gas, we initially set up the monomers of each chain to be stretched along  $z$ , separated by a distance equal to  $\sigma = 1$ . We let equilibrate for  $1e5$  steps, then keeping the surface at  $z = 0$  fixed, we lower the upper surface at an increment of size  $0.1\sigma$ , equilibrating for an additional  $1e5$  MD steps at each increment. Whenever an increment of 1 was reached, an additional equilibration of  $1e7$  MD steps was performed, and the final coordinates and velocities were saved to be used as initial conditions in the microscopic pressure tensor algorithm on C, where we ran the simulations for an additional  $1e7$  MD steps and collected



data at every 100 steps, such that we obtained  $1e5$  simulations to average over. A sample of the data obtained can be seen in figures 3.9 and 3.8.

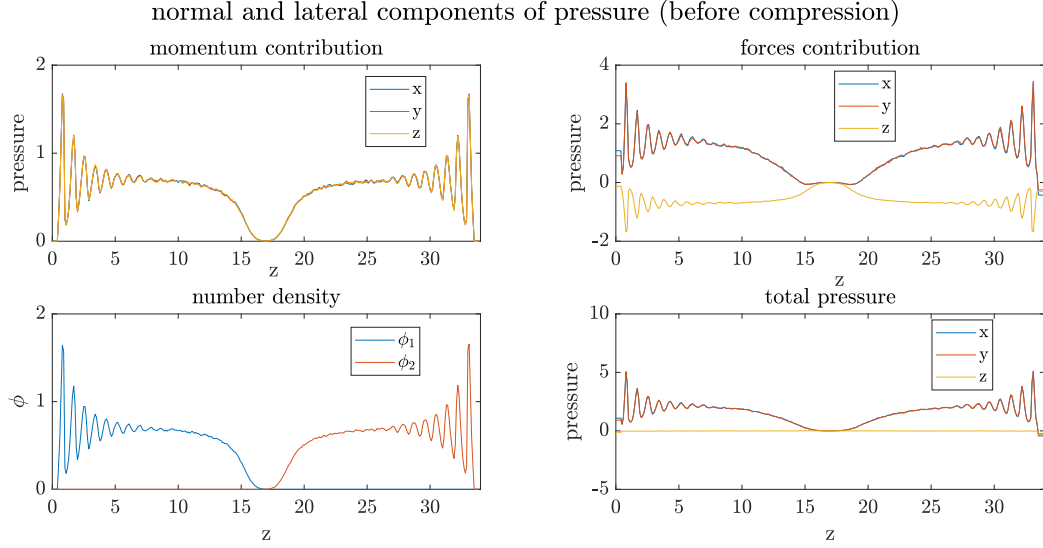


Figure 3.8: different components of the pressure tensor along the  $z$  axis for a monodisperse brush before interpenetration. The ideal contribution can be recovered from the momenta of the particles (top left), or equivalently from the density profile of the brush (bottom left). The forces contribution (WCA and KG) can be seen on the top right, and the total pressure due to both contributions on the bottom right.

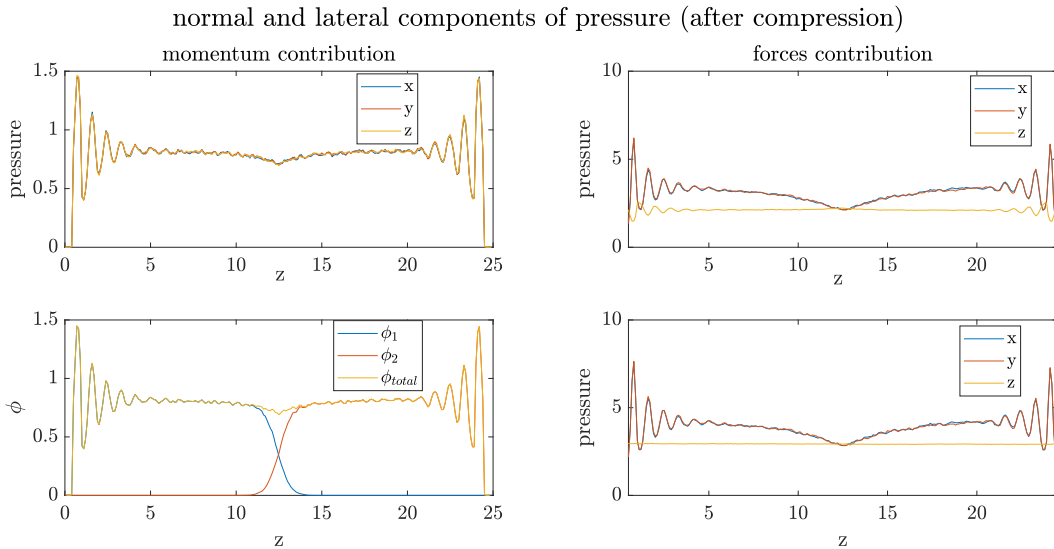


Figure 3.9: normal and lateral components of pressure tensor after compression. An interpenetration zone is established and the total pressure is positive.

The graphs perfectly matched our predictions; first of all, the ideal contribution to the pressure tensor was obtained using two approaches: the first by computing the momenta of the monomers, and the second by evaluating the local monomer density along the  $z$  direction. We find, as predicted, that the approaches are equivalent, and that the ideal pressure is indeed  $P_{ideal} = nk_B T$ . Second, we find that the force contribution along the  $z$ -axis is negative. This is to be expected; if there is no interpenetration, the momenta of all the degrees of freedom at equilibrium (minus that of the center of mass) must be cancelled out by a negative restoring force, which is accounted for through the KG non-ideal spring potential. By checking the numerical data, we find that these contributions are cancelled out up to 4 significant figures, which is of the order of the accuracy of our simulations. On the other hand, the forces (and total) contribution to pressure in  $x-y$  are positive due to the periodic boundary conditions, which impose external work on our system in these directions due to the image particles.

After compression (figure 3.8), the positive pressure is the osmotic pressure. We can clearly see that near the midplane, the pressure is isotropic. This shows that the system does behave like a polymer solution near this point.

As a final check, we also evaluate the pressure on the walls of the two grafting surfaces by computing the net force the walls exert on the rest of the system and dividing by the area of the surfaces ( $P = F/2A$ ). The result is shown in figure 3.10

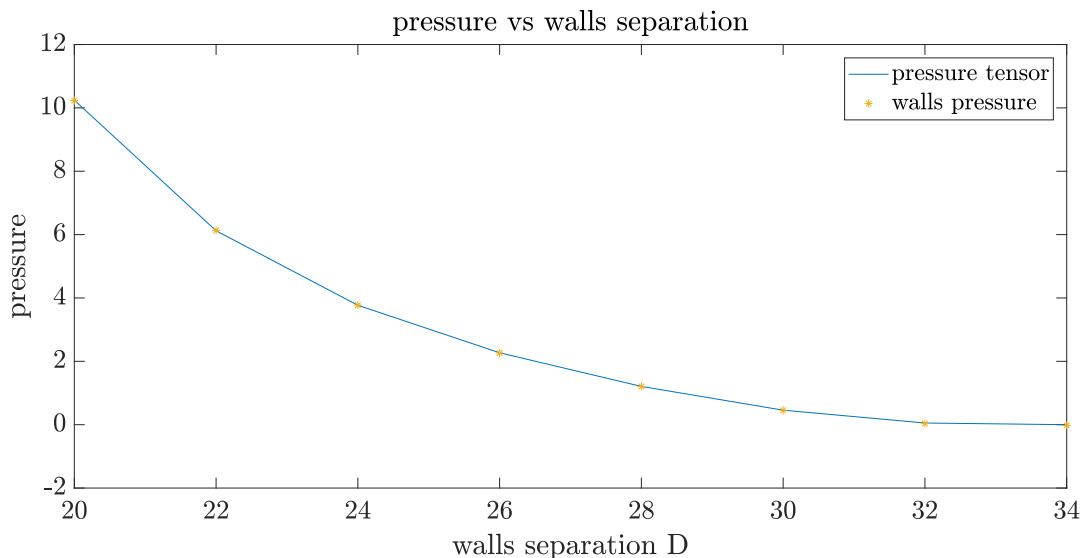


Figure 3.10: pressure computed from the microscopic pressure tensor (blue line), and from computing the net force exerted by the walls and dividing by the area of the surfaces (yellow points)

The same steps were repeated for brushes of polydispersity indices  $k = 1.05, 1.1, 2$ , with the only difference being that we take a larger number of chains ( $n_c = 100$ )

in order to ensure a proper sampling of the chain lengths distribution.

Having ensured that both the algorithm and system behaved as was expected, we then proceeded to verify the proposed theory that the free energy of a compressed bilayer is proportional to the energy of interbrush contacts.

### 3.2.3 Interaction Free Energy

We first attempt to verify the validity of the model in section 2.3.3. We check for two things: first of all, we investigate whether the number of interbrush contacts would indeed provide a good characterization of the free energy (and pressure) of the system. In that case, we expect a proportional relationship between these two quantities. Second of all, we verify the consistency of this model by seeing if things remain unchanged when we vary the polydispersity index.

For these purposes, we compress symmetric brush bilayers with different polydispersity indices  $k = 1, 1.05, 1.1, 2$ . The equilibration and data collection was conducted as described in the previous section. A "contact" was recorded whenever the distance  $d$  between two monomers belonging to opposite brushes was within the WCA potential range ( $0 < d \leq 2^{1/6}$ ). The interaction free energy was evaluated by taking the average pressure along the normal direction at each recorded separation. The data was then interpolated and fitted into a second degree polynomial, and finally integrated with respect to separation by using the trapezoidal method with integration step 0.5. The data for the number of contacts was also interpolated then fitted into a second degree polynomial. Figure 3.11 shows the results obtained.

From figure 3.11, we see that the interaction free energy is clearly proportional to the number of interbrush contacts. This shows that the assumption that the interaction free energy can indeed be characterized by such a local quantity does seem to be a valid one. However, although the assumed proportionality is confirmed, unexpected polydispersity effects appeared. To try and make sense of these findings, we investigate how pressure evolves not with the number of interbrush contacts, but with the minimum density along  $z$ . As explained in section 2.3, there is no stretching of the chains at the minimum in the density profile, and hence we expect the pressure to behave as it would in a semidilute solution. The corresponding results can be shown in figure 3.12.

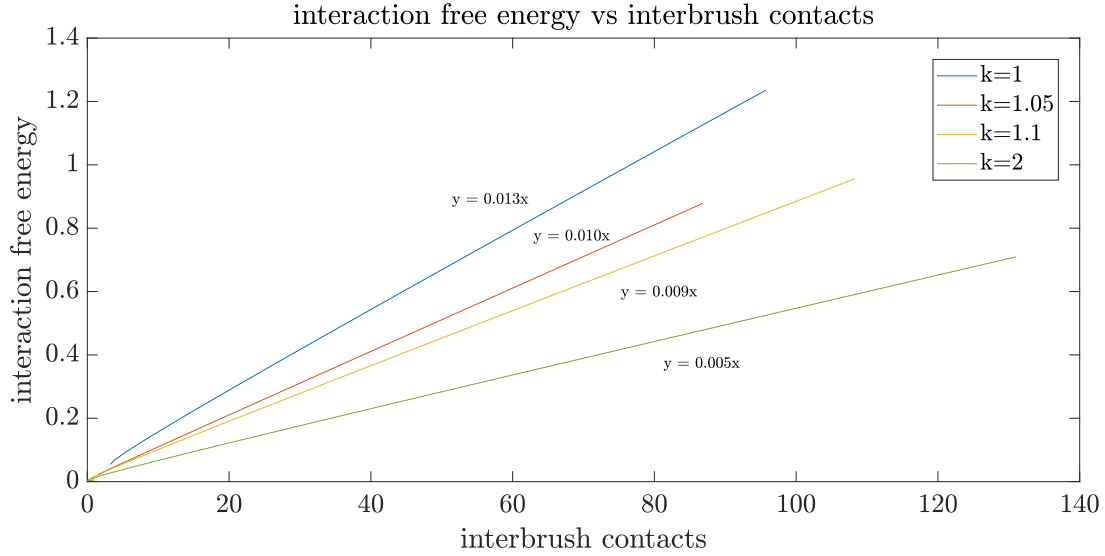


Figure 3.11: total interaction free energy vs number of interbrush contacts for brushes of polydispersity indices  $k = 1, 1.05, 1.1, 2$ . The maximum midplane density reached was about 0.6.

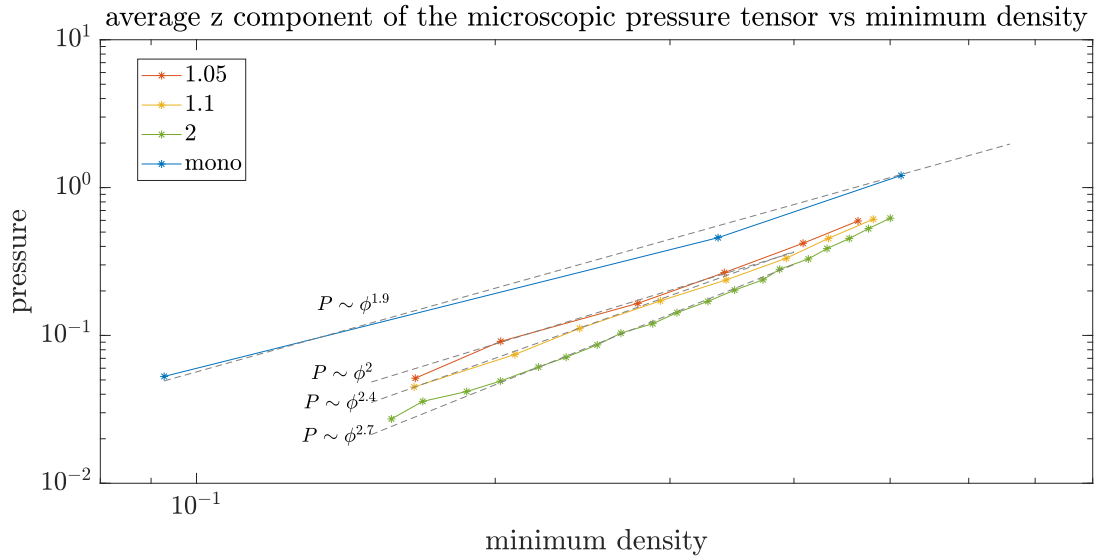


Figure 3.12: log-log plot of the average pressure vs the minimum density along  $z$

What we found was just as puzzling as before: in the semidilute regime (density range between 0.1 and 0.4), the dependence of pressure on density increased with polydispersity index. Additionally, the  $y$ -intercepts of these curves decreased with polydispersity index  $k$ , which implied that excluded volume interactions effectively depended on  $k$ . This relationship was not apparent in previous studies using numerical SCF and MC simulations [9], and had no clear explanation

within our framework, where the pressure is assumed to depend only on the local monomer density.

The natural next step was to check if this behaviour was due to some unaccounted-for effects in the brush bilayer, or to some other general effect which would emerge when we consider semidilute chain solutions.

### 3.2.4 Equation of State for Oligomers

We then consider a solution of oligomers in a cubic box with periodic boundary conditions in all directions, similar to our setting for the WCA gas. We study solutions of  $n_c = 9$  chains of lengths  $N = 2, 3, 5, 8, 10, 15, 20, 25, 100$ . As before, we initially set up the monomers on a lattice with separation  $\sigma = 1$ , and let the system relax for  $5e6$  steps. we then decrease the side lengths of the box by a step of 0.1, letting it equilibrate for an additional  $5e5$  steps then saving the final state of the system. We then use this data to run things for an additional  $5e6$  steps, collecting data for the pressure every 100 steps. We focus on the narrow density range of  $d = 0.1 - 0.2$  where we're definitely in the semidilute regime and higher order terms in the pressure are not significant. Finally, as we are interested mainly in studying the non-ideal contributions to pressure, we subtract from our total pressure (averaged over the  $z$  profile) the ideal contribution (which is due to the COM motion of the chains,  $P_{ideal} = kTn_c/V$ ). The result for some of the  $N$  studied is shown in figure 3.13.

We find that whatever effects were observed in the brush bilayer system were still apparent in the oligomer solution: the pressure plotted against the average density indeed follows a linear trend (with slope  $2.3 \pm 0.2$ ) as would be expected, but the curves were shifted by a constant, which again implies that the virial coefficient somehow must depend on the chain length  $N$ .

A possible conjecture that comes to mind is that chain ends might play a role; it is highly possible that those of the interior monomers in a chain, which are constrained on both sides, have smaller effective excluded volume than those at the end, which are constrained on only one. This effect should decrease with increasing  $N$ , where the fraction of chain ends becomes smaller, until it becomes negligible for long enough chains (which the mean field theory is based on). This hypothesis was backed by a study [28] in which the effect of chain length on pressure was studied at melt density. Linear chains were compared to ring polymers (which don't have ends). It was found that the pressure actually did depend on the molecular weight (length  $N$ ) in the case of a linear chain, but not in that of ring polymers, and the relationship was of the form  $P(N) - P_{(N \rightarrow \infty)} \propto N^{-1}$ , where  $P_{(N \rightarrow \infty)}$  is the pressure in the limit of very large  $N$ . This implied that the effect was indeed that of chain ends (As  $N$  increases, their fraction  $2/N$  decreases and chain end effects become negligible) Although our study was conducted in a different regime (semidilute as opposed to melt), this study motivated us to

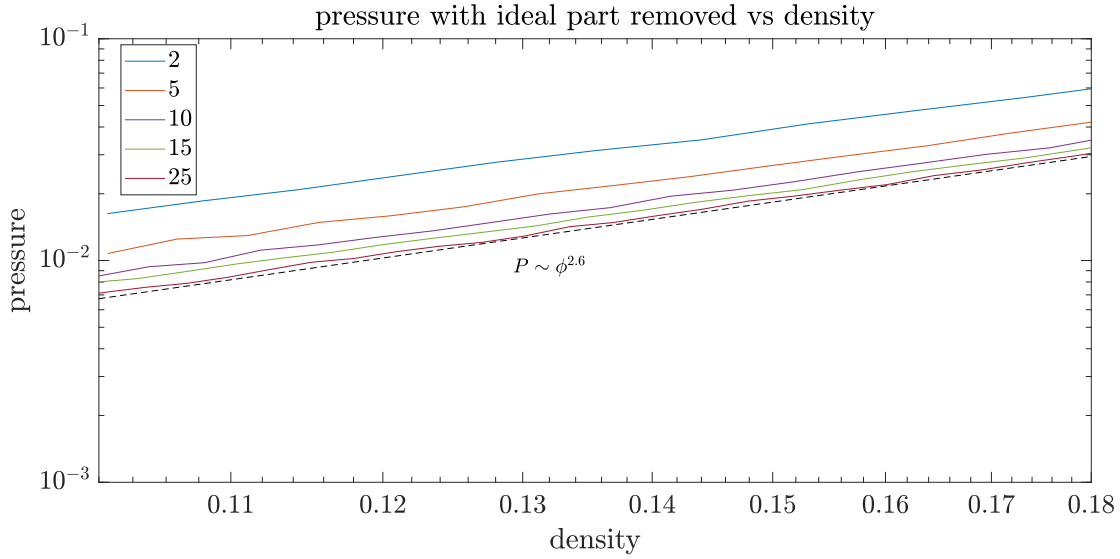


Figure 3.13: *log-log plot of the pressure vs the average density along  $z$  for a solution of  $n_c = 9$  chains of lengths  $N = 2, 5, 10, 15, 25$*

examine these effects more rigorously and attempt to relate our results to both their data at melt densities and our polymer brush system.

For this purpose, we start by checking if our results are consistent with those of the study. We gradually decrease the box size until we reach a density of  $\phi = 0.8$  and record the obtained pressure for different chain lengths. The results can be found in figure 3.14. We find that we did obtain the results in the paper, but with an downwards shift in pressure of about 0.2. The source of this small discrepancy remains unclear, but it could be possibly attributed to finite size effects.

As this pressure dependence is apparent in all regimes, we attempt to find an

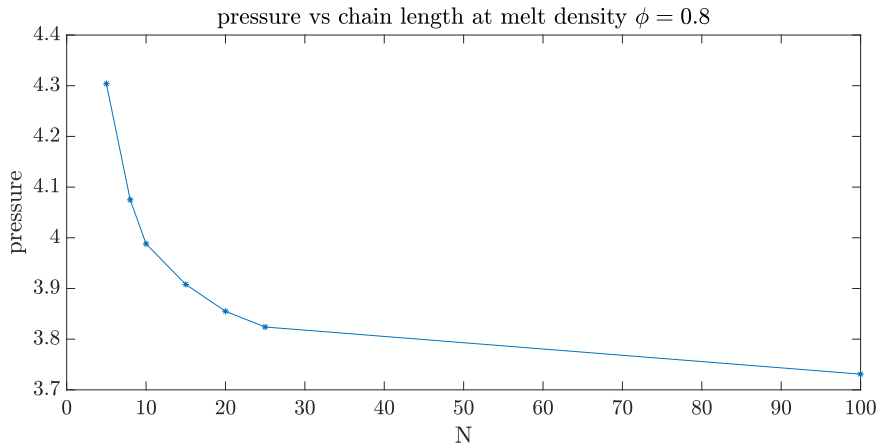


Figure 3.14: *Pressure vs chain length at melt density  $\phi = 0.8$*

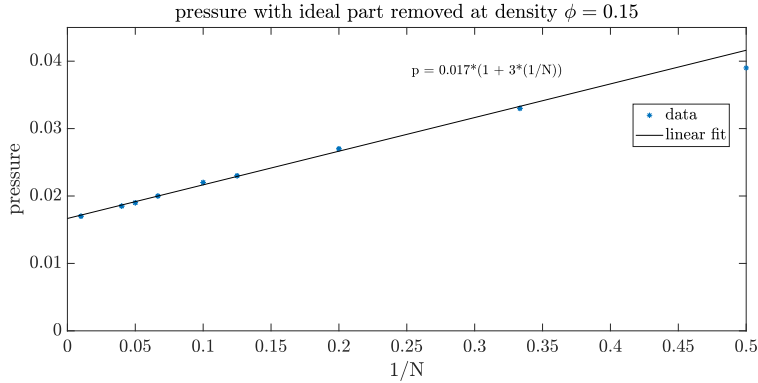
equation of state that would reproduce this behaviour for all densities. To make this system easier to compare with a brush bilayer, we remove the ideal gas contribution (by subtracting  $n_c/V$  from the total pressure). We find that in the regime we considered ( $\phi = 0.1 - 0.8$ ), the pressure has a linear dependence on  $1/N$ , which we fit into the following expression:

$$P(N) = P_{(N \rightarrow \infty)}(\phi)(1 + \alpha(\phi)(1/N)) \quad (3.2)$$

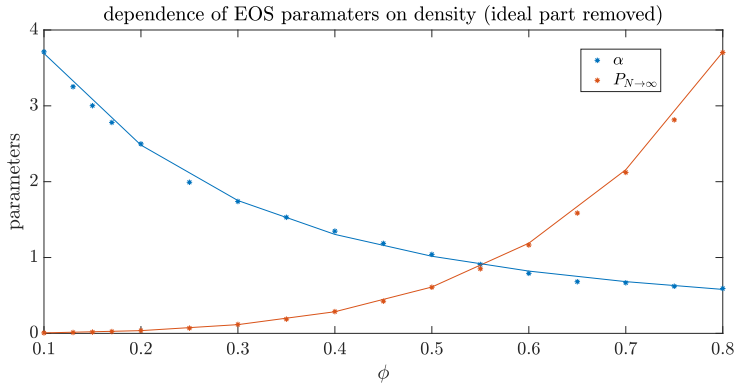
where  $\alpha$  is a dimensionless parameter. Figure 3.15a shows such a fit at  $\phi = 0.15$ . We find here that  $\alpha = 3.00 \pm 0.02$  and  $P_{(N \rightarrow \infty)} = 0.0167 \pm 0.0003$ .

We next try to see how  $\alpha(\phi)$  and  $P_{(N \rightarrow \infty)}$  would depend on the density of the system. The results can be summarized in figure 3.15b. We find that our data can be fit fairly well into polynomials of the form:

$$\begin{aligned} P_{(N \rightarrow \infty)} &= 1.1\phi^{2.3} + 5.4\phi^4 + 3.2\phi^6 \\ \alpha &= 0.05 + \frac{1}{0.2 + 2.36\phi^{1.5}} \end{aligned} \quad (3.3)$$



(a) pressure vs  $1/N$  for  $N = 2, 3, 5, 8, 10, 15, 20, 25, 100$  at average monomer density  $\phi = 0.15$



(b) dependence of the limiting  $P_{(N \rightarrow \infty)}$  and  $\alpha$  on the density in  $P(N) = P_{(N \rightarrow \infty)}(1 + \alpha(1/N))$

Having formulated this equation of state for polymer solutions, we attempt to map it to the equation of state of brush bilayers.

### 3.2.5 Chain End Effects in Brush Bilayers

Finally, we attempt to verify whether it was indeed the chain end effects that were responsible for the unexpected behaviour of pressure in our brush bilayer system. For this purpose, we run new simulations, this time for number average  $N_n = 15$  and number of chains  $n_c = 100$  for both brushes. The same equilibration and compression procedure as before was conducted. As we want to estimate the number of chain ends in the interpenetration zone, we extract the density profiles at each separation. The overlap  $\Gamma$  between the two brushes is simply the product of their respective density profiles ( $\Gamma = \phi_1(z)\phi_2(z)$ ). The interpenetration width can be extracted from fitting the overlap region with a good fitting model used in a recent study [9], given by

$$\Gamma = \left(\frac{\phi_0}{2}\right)^2 \cosh^2\left(\frac{z - z_0}{l}\right) \quad (3.4)$$

Where  $\phi_0$  is the central density along  $z$ ,  $z_0$  the distance from the  $z = 0$  surface where the maximum is found, and  $l$  is what we define to be the interpenetration length, which is equal to half the width of the fitted overlap region. A sample of this fit can be seen in figure 3.16 for  $k = 1.05$  and maximum density 0.0037 (note that it's the minimum density the overall profile). The fit wasn't as accurate around the edges, but this isn't necessary for our purposes.

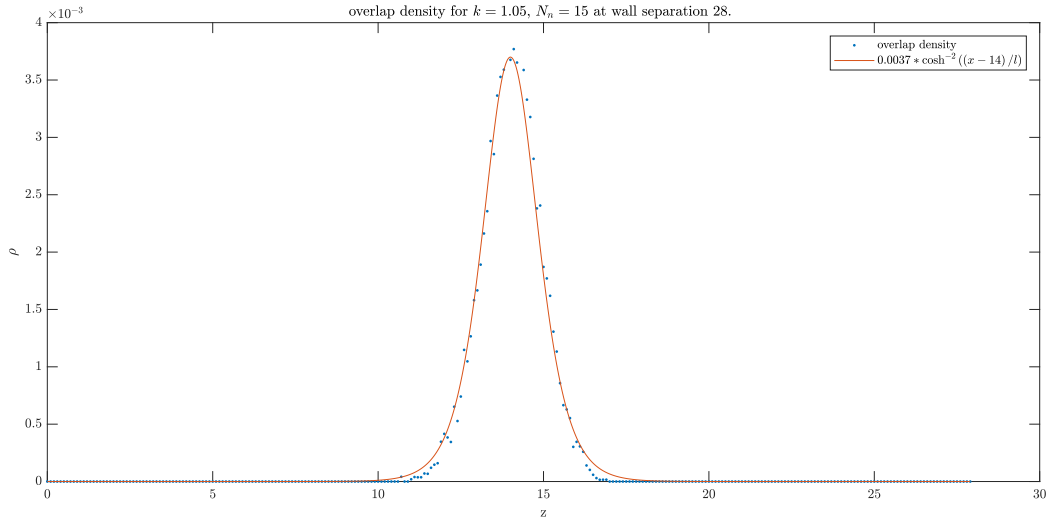


Figure 3.16: number density in the overlap region vs distance  $z$  from surface fitted using  $\Gamma = \left(\frac{\phi_0}{2}\right)^2 \cosh^2\left(\frac{z - z_0}{l}\right)$ , with  $\phi_0 = 0.12$  and  $z_0 = 14$

After fitting the overlap regions over the density range we're interested in (up to 0.3-0.4), we found that while the penetration length increased with polydispersity



index ( $l = 0.5, 1, 1.5, 2.5$  for respective polydispersity indices  $k = 1, 1.05, 1.1, 2$ ), it remained constant throughout the compression, which made it easy to account for in the simulations (figure 3.17). We therefore ran our simulations again, this time while counting the number of chain ends found within the width of penetration (within the range  $[z_0 - l; z_0 + l]$ ).

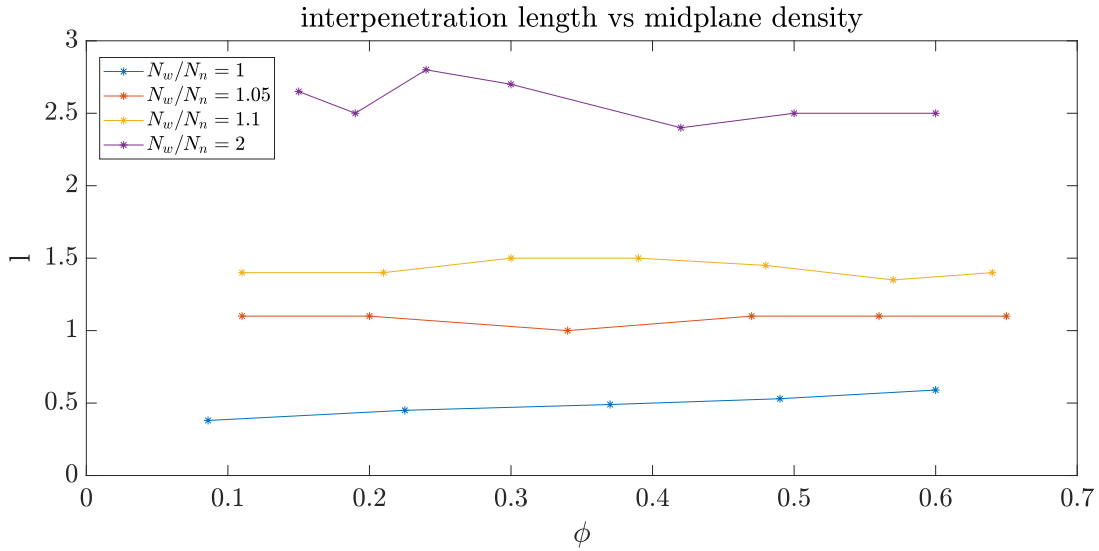


Figure 3.17: interpenetration length  $l$  vs minimum density in the brush profile.

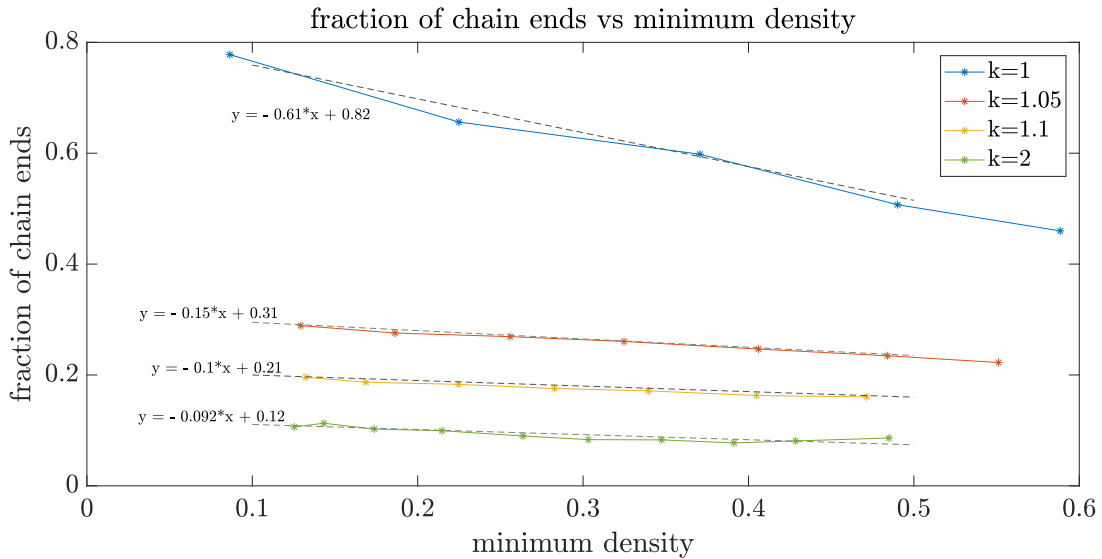


Figure 3.18: fraction of chain ends in the interpenetration zone vs the minimum density along  $z$  for  $k = 1, 1.05, 1.1, 2$

Our results are shown in fig 3.18. We can clearly see that the fraction of chain

ends actually drops with the polydispersity index, which is consistent with our previous observation that the normal pressure decreases with increasing  $k$ . We then see if the corresponding pressures would match those of the chain solutions at the same fraction of chain ends. For this purpose, we fit the data in figure 3.18 into a straight line to extract the fraction at densities 0.1-0.4 in steps of 0.1. We also fit the pressure vs density data into a second degree polynomial in this same range and extract the corresponding pressure. The results are shown in figure 3.19. We see that the data points from the brush bilayer match reasonably well with the equation of state from the polymer solutions, except in the monodisperse case (data point of the largest fraction of chain ends), with a downwards shift of about 10 – 12%. The possible sources of these discrepancies are still unclear and require more investigations in the future. Finally, we verify if our equation of state

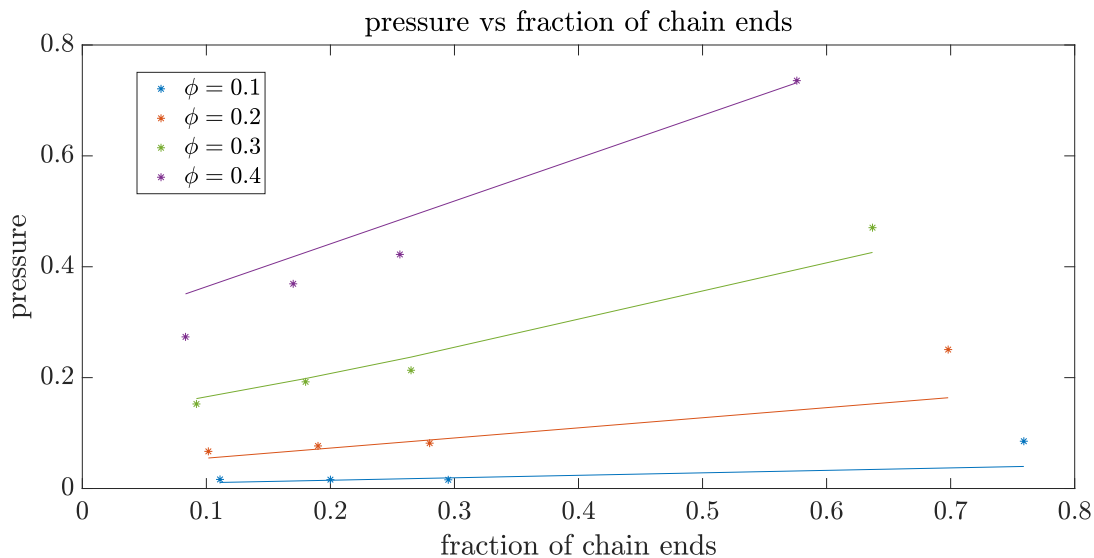


Figure 3.19: pressure vs fraction of chain ends in polymer solutions (solid lines) and brush bilayers (stars)

obtained from the polymer solutions would predict the dependence of pressure on minimum density for brush bilayers. The result is shown in figure 3.20. We find that while the points don't match perfectly well with the equation of state of polymer solutions, we do get the appropriate trend and a decent prediction of the equation of state of brush bilayers. More studies should be conducted to improve these results.

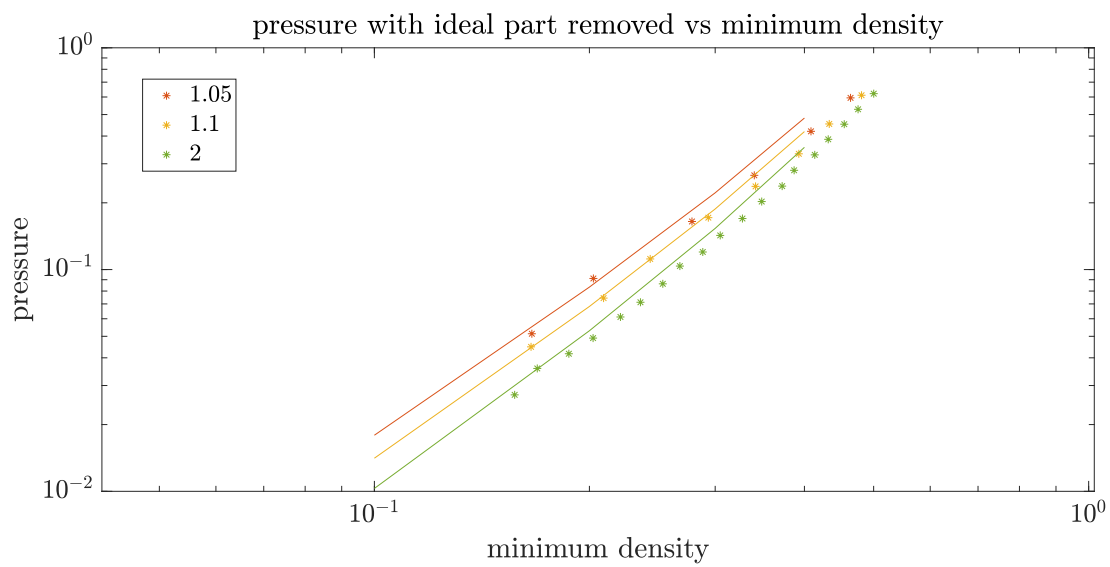


Figure 3.20: pressure vs minimum density in polymer solutions (solid lines) and brush bilayers (stars)

### 3.3 Conclusions and Future Work

We have performed molecular dynamics simulations on the monodisperse brush for different chain lengths and showed that there is no evidence of coupling of the degrees of freedom in such a system, which is an indication that the entanglement effects are not apparent in the regime of short ( $N < 30$ ) chains grafted at low grafting densities ( $\sigma = 0.11$ ). While we did recover the predictions within the framework of the Rouse model for a monodisperse brush, we were not so successful in the polydisperse case. Part of the problem could be attributed to surface effects, which become prominent when looking at short chains ( $N < 10$ ). However, our data suggests that other artefacts might be coming into play: because of polydispersity, chains of the same length would be subject to different fields, thus affecting their dynamics. We would then be averaging over a system with frozen disorder, and not exploring properly the entirety of the configuration space available to the chain. Many checks could be done in future works to verify this hypothesis: one could start with a sample at very low grafting density  $\sigma$ , such that the individual chains do not feel their neighbours. The relaxation dynamics should follow then the predictions of the Rouse model. We could then gradually increase  $\sigma$  and see how the relaxation times are affected. Another check to do would be to explore a larger range of polydispersity indices and see how things change in the limits of very low ( $k = 1.01$ ) and very high ( $k = 2$ ) polydispersity indices.

We have also performed molecular dynamics simulations on a brush bilayer system to characterize its compressive pressure and interaction free energy. We have found that both the pressure and the interaction free energy were proportional to the number of interbrush contacts, although there doesn't seem to be a solid argument that explains why this relationship would exist. However, our studies revealed an effect of polydispersity on pressure that was not accounted for in any of the previous theories and models for brushes. This effect was also apparent when looking at the pressure dependence on the minimum density. After investigating the relationship further, we discovered that these effects were due to the energetic contributions of end monomers in a chain being different from those of the middle monomers. Indeed, we found that the fraction of end monomers consistently decreases with increasing polydispersity. We then systematically studied the dependence of pressure on fractions of chain ends with solutions of oligomers, and extrapolated our results to match those for melt densities found in the literature. We finally used the equations of state obtained from oligomer solutions to predict the pressure dependence on polydispersity with reasonable success. This work could be taken a step further both computationally by exploring how these effects vary with average chain lengths and grafting densities (where we expect them to be less significant), and theoretically, possibly by introducing the idea of a virial coefficient for chain ends different from the virial coefficient of middle monomers.

# Bibliography

- [1] I. Teraoka, *Polymer solutions: an introduction to physical properties*. Wiley, 2002.
- [2] S. Qi, L. I. Klushin, A. M. Skvortsov, and F. Schmid, “Polydisperse polymer brushes: Internal structure, critical behavior, and interaction with flow,” *Macromolecules*, vol. 49, no. 24, p. 9665–9683, 2016.
- [3] T. Kreer and S. Balko, “Scaling theory for compressed polymer-brush bilayers,” *ACS Macro Letters*, vol. 2, p. 944–947, Apr 2013.
- [4] T. Kreer, “Polymer-brush lubrication: a review of recent theoretical advances,” *Soft Matter*, vol. 12, no. 15, p. 3479–3501, 2016.
- [5] L. I. Klushin and A. M. Skvortsov, “Critical dynamics of a polymer chain in a grafted monolayer,” *Macromolecules*, vol. 24, no. 7, p. 1549–1553, 1991.
- [6] M. Murat and G. S. Grest, “Structure of a grafted polymer brush: a molecular dynamics simulation,” *Macromolecules*, vol. 22, no. 10, p. 4054–4059, 1989.
- [7] K. Binder, “Scaling concepts for polymer brushes and their test with computer simulation,” *The European Physical Journal E*, vol. 9, no. 3, p. 293–298, 2002.
- [8] D. Reith, A. Milchev, P. Virnau, and K. Binder, “Computer simulation studies of chain dynamics in polymer brushes,” *Macromolecules*, vol. 45, p. 4381–4393, Oct 2012.
- [9] L. I. Klushin, A. M. Skvortsov, S. Qi, T. Kreer, and F. Schmid, “Polydispersity effects on interpenetration in compressed brushes,” *Macromolecules*, vol. 52, no. 4, p. 1810–1820, 2019.
- [10] G. A. and A. Khokhlov, *Statistical physics of macromolecules*. AIP Press, 2002.
- [11] M. Rubinstein and R. H. Colby, *Polymer physics*. Oxford University press, 2016.

- [12] P. J. Flory and W. R. Krigbaum, “Thermodynamics of high polymer solutions,” *Annual Review of Physical Chemistry*, vol. 2, no. 1, p. 383–402, 1951.
- [13] G. C. Rutledge, “Polymer solution thermodynamics.”
- [14] R. A. L. Jones, *Soft condensed matter*. Oxford University Press, 2014.
- [15] F. P. Chinard, “The definition of osmotic pressure,” *Journal of Chemical Education*, vol. 31, no. 2, p. 66, 1954.
- [16] S. Rathgeber, “Johannes gutenbergs-university mainz - userpages.”
- [17] D. Marsh, “Scaling and mean-field theories applied to polymer brushes,” *Biophysical Journal*, vol. 86, no. 4, p. 2630–2633, 2004.
- [18] S. T. Milner, T. A. Witten, and M. E. Cates, “A parabolic density profile for grafted polymers,” *Europhysics Letters (EPL)*, vol. 5, p. 413–418, Jan 1988.
- [19] S. T. Milner, “Polymer brushes,” *Science*, vol. 251, no. 4996, p. 905–914, 1991.
- [20] G. S. Grest, “Normal and shear forces between polymer brushes,” *Polymers in Confined Environments Advances in Polymer Science*, p. 149–183, 1999.
- [21] W. Hu, *Polymer physics: a molecular approach*. Springer, 2013.
- [22] P. Lai and K. Binder, “Structure and dynamics of grafted polymer layers: A monte carlo simulation,” *The Journal of Chemical Physics*, vol. 95, no. 12, p. 9288–9299, 1991.
- [23] G. V. Schulz *Z.Z. Phys. Chem. (Munich)*, vol. 44B, no. 1, 1939.
- [24] B. H. Zimm, “Apparatus and methods for measurement and interpretation of the angular variation of light scattering; preliminary results on polystyrene solutions,” *The Journal of Chemical Physics*, vol. 16, no. 12, p. 1099–1116, 1948.
- [25] P. Schofield and J. Henderson, “Statistical mechanical of inhomogeneous fluids,” *Proceedings of the Royal Society of London*, vol. 379, no. 1776, p. 231–246, 1982.
- [26] J. H. Irving and J. G. Kirkwood, “The statistical mechanical theory of transport processes. iv. the equations of hydrodynamics,” *The Journal of Chemical Physics*, vol. 18, no. 6, p. 817–829, 1950.

- [27] S. Hess, “Augmented van der waals equation of state for the lennard-jones fluid,” *Physica A: Statistical Mechanics and its Applications*, vol. 267, no. 1-2, p. 58–70, 1999.
- [28] C. Meddah, A. Milchev, S. A. Sabeur, and A. M. Skvortsov, “Molecular weight effects on interfacial properties of linear and ring polymer melts: A molecular dynamics study,” *The Journal of Chemical Physics*, vol. 145, no. 19, p. 194902, 2016.